NASA CR-170578

ERT
A COMSAT COMPANY
ENVIRONMENTAL RESEARCH & TECHNOLOGY, INC.
ATLANTA · CHICAGO · CONCORD, MA · DENVER · FORT COLLINS, CO
HOUSTON · LOS ANGELES · PITTSBURGH · WASHINGTON, DC

IMPACT OF SATELLITE DATA ON LARGE-SCALE CIRCULATION STATISTICS AS DETERMINED FROM GLAS ANALYSES DURING FGGE SOP-I

David A. Salstein[1]
Richard D. Rosen[1]

Final Report on Contract NAS5-26515
Environmental Research & Technology, Inc.
696 Virginia Road
Concord, Massachusetts 01742

December 1982

[1]Present address: Atmospheric and Environmental Research, Inc.
840 Memorial Drive, Cambridge, Massachusetts 02139

1. Introduction

The state of the atmosphere, as determined from analyses of meteorological data, can be examined in detail for a certain time period in order to generate statistics related to the global budgets of momentum, heat, and water vapor. Studies using analyses derived from the assimilation-forecast cycle of a general circulation model (e.g., Rosen and Salstein, 1980, using NMC global analyses) have done so for periods of up to a season. Recently, a variety of data from satellite observing systems have supplemented the routine surface-based data in order to produce gridded analyses that are considered to be superior to those preceding them. Thus, the general circulation statistics from these analyses may be improvements over past sets.

In order to understand results based on analyses from differing input data sets we have undertaken a study using the analyses produced from the assimilation cycle of parallel model runs that both include and withhold satellite data. Furthermore, because the basic statistics from any model-based analysis must be put into perspective, we do so by comparing statistics with those obtained by a traditional approach as used by Oort and Rasmusson (1971). This study is, therefore, a three-way comparison of the analyzed state of the atmosphere, and it is performed using data from a certain test period during the first Special Observing Period (SOP) of the Global Weather Experiment (FGGE). The three analyses are denoted as follows:

(1) "FGGE" - the global analysis from the assimilation mode of the NASA Goddard Laboratory for Atmospheric Sciences (GLAS) General Circulation Model incorporating all available types of incoming data during the 6 January - 4 February 1979 period from the FGGE level II-b database (see Baker et al., 1981). We are examining the 30-day average (hereafter called a "monthly" average) of these daily analyses at 00 GMT from the 4° x 5° latitude-longitude grid.

(2) "NOSAT" - the GLAS gridded analyses for the same period, but based on a restricted set of incoming data sources. Data from satellites as well as from some special observing systems were omitted (see Table 2 of Halem et al., 1982).

(3) "STATION" - traditional analysis of the monthly period based on rawinsonde and pilot balloon data alone in the manner of the station analysis in Rosen and Salstein.

2. Data and Initial Processing

a. Gridded Data

From NASA we requested and received monthly sums of certain meteorological parameters and their cross products for every point on the 4° x 5° latitude-longitude global grid. Latitudes of the grid run from the South Pole to the North Pole, and there are twelve pressure levels ranging from 1000 to 50 mb. Details of the grid, as well as a list of the parameters can be found in Attachment A. Two data tapes were received representing independently the FGGE and NOSAT cases.

b. Station Data

We also received from NASA data tapes containing rawinsonde and pilot balloon (pibal) station data from the same FGGE level II-b data base. Up to 13 levels including the surface are available for the atmosphere up to 50 mb, and at these levels, height (z), temperature (T), relative humidity (RH), and the eastward and northward components of the wind (u and v) can appear, as well as quality marks for each of these.

The effort necessary to create monthly average values of parameters and their cross products at individual levels for the set of stations is summarized in the flow chart of Figure 1. From the data tape, a station record is examined for its WMO number, exact observation time, and data source type (rawinsonde or pibal). A recurring problem is the following: The same WMO number can appear on more than one record (report) for the 00 Z synoptic file. Often it is the case that the winds appear as a pibal report while the other meteorological parameters are on a rawinsonde report. In this case, the two sets of observations were "merged". However, multiple records of the same source type also do appear, usually from observations made at different times, but close enough to 00 Z to be included on the file. In such a case, the better of the "duplicate" stations was selected according to the following order of objective

criteria: (1) reporting the same hour as its corresponding pibal/rawinsonde "merging" partner, if one exists, (2) having the greater number of levels, or (3) being closest to 00 Z in reporting time.

All data are examined for any errors which may appear. A datum was discarded if its associated quality code was >2 (indicating an erroneous value), or if it exceeded the gross error checks listed in Attachment B. Covariance matrices are formed from the available data, and after a day's records are read, the parameters, cross products and population information are added to accumulating sums. At the end of the month the covariance tape is written.

Data were collected in the above manner for all land-based stations, and certain ship stations which were relatively stationary during the month and so considered "fixed". In addition, some Tropical Wind Observing Ships (TWOS) were also discovered to be stationary enough to be used in this study. Data to create covariance sums for these TWOS ships were obtained separately from NOAA, Asheville, The call letters and locations of all fixed ships are listed in Table 1.

A monthly average value or covariance from the stations is used in our analysis only if it passes the cut-off criterion, which is as follows: (i) it is based on $\geq$15 observations (out of 30 possible) north of 30° N, or (ii) it is based on $\geq$10 observations south of 30°N. We have lowered the criterion south of 30° N because of (i) the lower expected temporal variance at locations in the tropics and (ii) the need for as many stations as possible to be used in the data sparse areas. As a result of variable reporting and the use of these criteria, a somewhat different set of stations goes into the analysis of each quantity. We choose to show the distribution at 850 mb of stations with sufficient observations of (i) wind and temperature (Figure 2a) and (ii) humidity (Figure 2b).

3. Formation and Display of Basic Horizontal Fields and Latitude-Height Cross Sections

In the STATION data, Northern Hemisphere horizontal analyses for the basic quantities are created at each level on a polar stereographic grid (see Rosen et al., 1979, for a description of this horizontal analysis). We have chosen to present some time-averaged fields at one low level (850 mb) and one high level (200 mb) in order to illustrate some similarities and differences amongst the three analyses. The horizontal

fields from the STATION analysis are moved onto an equidistant Mercator projection for display purposes and for comparison with the FGGE and NOSAT analyses.

Figure 3 shows the monthly average of u, written as $\bar{u}$, at 850 mb for the (a) FGGE, (b) NOSAT and (c) STATION analysis. (Note the restriction of the STATION field to the Northern Hemisphere.) $\bar{v}$ at 850 mb appears in Figure 4, $\bar{T}$ (°C) at 850 mb in Figure 5, $\bar{q}$ (specific humidity) at 850 mb in Figure 6, $\bar{u}$ at 200 mb in Figure 7, and $\bar{v}$ at 200 mb in Figure 8. All fields obtained from the GLAS analyses, as well as subsequent analyses, are restricted here to the portion of the globe north of 68°S. Southward of that latitude the high topography of Antarctica affects the low-level fields.

In the next step towards diagnosing the general circulation, zonal averages (notated here using surrounding brackets) of the basic quantities were generated. For the gridded analyses, we have computed such averages around all latitude circles from 66°S to 86°N latitude at the 12 pressure levels. Values are then put on a cross-sectional grid spaced every 50 mb in the vertical and 4° in latitude. At those levels where zonal averages are not performed directly, values are obtained by interpolation from surrounding levels. For the STATION analysis, zonal averages are formed from values at grid points of the Northern Hemisphere horizontal analysis which fall within certain zonal bands. From these, cross-sectional fields are created on a grid of 50 mb x 4°, as in the FGGE and NOSAT cases.

Fields of $[\bar{u}]$ for the FGGE, NOSAT and STATION cases are presented in Figure 9, as are fields of $[\bar{v}]$, resulting mass streamfunction, $\bar{\Psi}$, and $[\bar{T}]$ in Figures 10, 11, and 12 respectively. The Northern Hemisphere maxima in $[\bar{u}]$ occur at 30° and 200 mb, and are found to be stronger in the NOSAT case than the FGGE case, and weakest in the STATION analysis (Figure 9). Indeed this seems to be the case for some regions in Figure 7. By and large, all three analyses appear to be rather similar in Figure 7, although the NASA GLAS analyses have more structure over the oceans and other data-sparse areas than does the STATION analysis.

The meridional flow and associated mass streamfunctions from the three analyses show similar properties. Despite the difficulties in analyzing time-mean meridional motions, the analyses of $\bar{v}$ are quite

similar in structure. One might have expected the satellite systems to have more impact than was found. The Hadley cell in the tropics of Figure 11, though, is strongest in the NOSAT analysis, only a little weaker in the FGGE analysis, and weakest in the STATIONS.

The three results for $[\bar{T}]$ are similar with the greatest difference appearing at the 50 mb level where some very cold values occur in the tropics in the NOSAT analysis. Though qualitatively very similar, there are some differences in Figure 5 between the FGGE and NOSAT analyses, particularly in the Southern Hemisphere. The analyses of $\bar{q}$ in the three cases are also very close although some regions show differences. Zonal averages of $\bar{q}$ at 850 mb are plotted in Figure 13.

4. Momentum and Heat Calculations

a. Momentum Fluxes and Kinetic Energy Conversions

The total northward flux of angular momentum has been partitioned into that by the mean meridional cell and by eddy components. This decomposition is given by

$$2\pi a^2 g^{-1} \int [\overline{uv}] \cos^2\phi dp = 2\pi a^2 g^{-1} \left\{ \int [\bar{u}][\bar{v}] \cos^2\phi dp + \int [\overline{u'v'}] \cos^2\phi dp + \int [\bar{u}^*\bar{v}^*] \cos^2\phi dp \right\}$$

where a is the radius of the earth, g gravitational acceleration, ϕ latitude, p pressure, an overbar denotes monthly mean, a prime denotes deviation from the monthly mean, brackets denote zonal mean and an asterisk denotes deviations from the zonal mean of a quantity. The right hand side represents the contributions to the total momentum flux by the mean meridional circulation (MMC), the transient eddies (TE) and the standing eddies (SE), in that order. The latitudinal profiles of the three parts of the northward momentum flux for the FGGE, NOSAT and STATION cases are shown in Figure 14a-c. The largest distinctions are seen in the MMC, which is usually rather difficult to measure.

A picture of the differences in the momentum flux by the transient eddies is shown in Figure 15, with the NOSAT case having the highest peaks. In order to look at the regions where the differences appear, the latitude-height cross sections $[\overline{u'v'}]$ are shown in Figure 16.

Again the value in the NOSAT case exceeds that of FGGE in the regions of maximum values, near 300 mb, 30°N, and 200 mb, 30°S. Both are also larger than the STATION case in the Northern Hemisphere. To look further at some regional origins of these differences, values of the horizontal field $\overline{u'v'}$ at 200 mb are displayed in Figure 17. Some areas of difference which stand out are in the North Pacific Ocean. Also shown are cross-sections of $[\bar{u}^*\bar{v}^*]$ in Figure 18 which contain some of the differences amongst the three cases.

The kinetic energy of the global atmosphere is computed from the three cases, and can be partitioned into its mean, TE and SE forms, as follows:

$$K_M = \tfrac{1}{2} \int ([\bar{u}]^2 + [\bar{v}]^2)\, dm$$

$$K_{TE} = \tfrac{1}{2} \int ([\overline{u'^2}] + [\overline{v'^2}])\, dm$$

$$K_{SE} = \tfrac{1}{2} \int ([\bar{u}^{*2}] + [\bar{v}^{*2}])\, dm$$

where $dm = g^{-1} 2\pi a^2 \cos\phi \, d\phi \, dp$

Kinetic energy is converted from eddy to zonal mean state by the action of the eddy fluxes of momentum. The conversion can be given by the formula

$$C(K_E, K_M) = 2\pi a^2 g^{-1} \int\int ([\overline{u'v'}] + [\bar{u}^*\bar{v}^*]) \frac{\partial}{\partial\phi} \left(\frac{[\bar{u}]}{a\cos\phi}\right) \cos^2\phi \, d\phi \, dp$$

$$= C(K_{TE}, K_M) + C(K_{SE}, K_M)$$

Energy terms and conversion terms for both hemispheres are given in Table 2.

In addition we have calculated values of the conversion from zonal mean available potential energy to zonal mean kinetic energy. It can be approximated by

$$C(P_M, K_M) = 2\pi a^2 g^{-1} \int\int 2\Omega [\bar{u}][\bar{v}] \sin\phi \cos\phi \, d\phi dp$$

where Ω is the rotation rate of the earth. Values for the three analyses are also included in Table 2.

b. Heat Fluxes and Potential Energy Conversions

Analogous to the flux of angular momentum in the atmosphere is the northward flux of heat, which likewise can be partitioned into mean meridional cell and eddy components by the expression

$$2\pi a\, g^{-1} \cos\phi \int C_p[\overline{vT}]\, dp = 2\pi a\, g^{-1} \cos\phi \left\{ \int C_p[\bar{v}][\bar{T}]\, dp + \int C_p[\overline{v'T'}]\, dp + \int C_p[\bar{v}^*\bar{T}^*]\, dp \right\}$$

where C_p is the specific heat of air at constant pressure.

In an analogous manner, we have also displayed in Figure 19 the latitudinal profile of the three components of heat flux, that by the transient eddies (in expanded scale) in Figure 20, cross-sections of $[\overline{v'T'}]$ in Figure 21, values of $\overline{v'T'}$ at 850 mb, the level of its maximum (Figure 22) and cross-sections of $[\bar{v}^*\bar{T}^*]$ in Figure 23. Despite the very strong similarities in the two NASA GLAS analyses which are found in these figures, some differences can be pointed to, particularly in the Southern Hemisphere.

The potential energy atmospheric values can be given as

$$P_M = \frac{C_P}{2} \int \gamma \left([\bar{T}]''\right)^2 dm \quad \text{where } [\bar{T}]'' = [\bar{T}] - \int_0^{\pi/2} [\bar{T}] \cos\phi\, d\phi$$

$$P_{TE} = \frac{C_P}{2} \int \gamma\, [\overline{T'^2}]\, dm$$

$$P_{SE} = \frac{C_P}{2} \int \gamma\, [\bar{T}^{*2}]\, dm$$

γ is related to the static stability factor, computed from the temperature field. The eddy fluxes of heat convert potential energy from the zonal form P_M to an eddy form, as follows:

$$C(P_M,P_E) = -2\pi a\, g^{-1} \int\int \gamma \left(C_p[\overline{v'T'}] + C_p[\bar{v}^*\bar{T}^*]\right) \frac{\partial}{\partial\phi}[\bar{T}] \cos\phi\, d\phi\, dp$$

$$= C(P_M,P_{TE}) + C(P_M,P_{SE})$$

Values for both hemispheres of these terms will be found in Table 2.

5. Final Remarks

The chief aim of this work has been to examine the influence that "non-conventional" data, derived from satellite-based observation systems, have on atmospheric analyses. Although this impact has been studied previously with regard to short-range weather forecasts, this is the first time that the influence on general circulation statistics has been examined. It is also one of the first studies of the general circulation through the depth of the Southern Hemisphere. We have chosen to study a period when extensive observations of all types were collected, that is, one month during the Global Weather Experiment (FGGE).

We have discovered though that the two analyses during this period yield many similarities as well as differences. The basic influence of the satellite systems seem to be a reduction in the magnitude of the winds. This is perhaps due to the insertion of satellite data at a much denser network than is available from the NOSAT network. The overall distinction between the FGGE and NOSAT cases also does not seem large when examined in comparison with the traditional STATION analyses. Prior estimates of the atmosphere's energy cycle may thus have to be revised after incorporating data from more types of sources. When examining these figures, it is important to remember also that the NOSAT analysis had aircraft data available to it which the STATION analysis did not. This fact may be particularly clear, for example, when examining the large maxima in the $\overline{u'v'}$ field at 200 mb in the North Pacific, which is a busy air route. Nevertheless, Table 2 shows that the integrated effect on the energy and conversion terms are sufficiently different between the FGGE and NOSAT cases to suggest that satellite data have had an impact, although we might have expected it, a priori, to be greater.

In addition, an important question to examine is the influence of the particular model's analyses on such statistics. We examined the objective analysis output from the 4th order 4° x 5° GLAS GCM. The statistics from these analyses are compared with those resulting independently from a traditional approach. Modification of the analysis scheme, such as the use of an optimum interpolation method, might produce

significant differences in these statistics as well. As such, it would also be important to examine statistics based on future modifications to estimate model influences. The influence of the model characteristics themselves could be examined as well with output from a long model run. A further discussion of these points and the results and figures presented here can be found in Salstein et al. (1983).

References

Baker, W., D. Edelmann, M. Iredell, D. Han and S. Jakkempudi, 1981: Objective analysis of observational data from the FGGE observing systems, NASA Technical Memorandum 82062, NASA Goddard Space Flight Center, Greenbelt, MD 20771, 132 pp.

Halem, M., E. Kalnay, W. Baker and R. Atlas, 1982: An assessment of the FGGE satellite observing system during SOP-1, Bull. Am. Meteor. Soc., 63, 407-426.

Oort, A.H. and E.M. Rasmusson, 1971: Atmospheric Circulation Statistics. NOAA Prof. Pap. No. 5, 323 pp. [NTIS COM-72-50295].

Rosen, R.D., D.A. Salstein and J.P. Peixoto, 1979: Variability in the annual fields of large-scale atmospheric water vapor transport, Mon. Wea. Rev., 107, 26-37.

Rosen, R.D. and D.A. Salstein, 1980: A comparison between circulation statistics computed from conventional data and NMC Hough analyses, Mon. Wea. Rev., 108, 1226-1247.

Salstein, D.A., R.D. Rosen, W. Baker and E. Kalnay, 1983: Impact of satellite data on diagnoses of large-scale circulation statistics, manuscript in preparation.

Table 1

Call Letters and Location of Ships Used in Study

Call Letter	Mean Latitude	Mean Longitude (West)
1. Standard Ship Reports		
C7C	52.70	35.50
C7L	56.60	17.00
C7M	65.80	358.00
C7P	50.00	145.00
C7R	47.10	17.00
DBBH	.40	22.00
EREC	2.90	253.10
EREH	2.20	274.00
EREI	4.40	270.00
ERES	5.00	29.00
FNBG	1.00	4.00
JBOA	39.00	223.70
[illegible]P1	74.80	169.90
TOFI	4.50	15.10
UEAK	2.50	220.00
UHQS	.00	252.50
UMAY	.00	270.10
UMFW	-51.00	332.50
2. Tropical Wind Observing Ships		
CAMAR	2.60	46.00
DRAGA	7.25	42.52
GAKKE	4.87	23.52
LOMON	8.17	23.46
MANUS	-2.07	212.57
PARIZ	- .47	151.20
PRACT	-3.14	187.73
RESEA	-2.27	26.08
SALDA	1.46	40.60
SAMOI	4.95	35.00
TTRS9	2.30	197.17

Table 2

Energy terms (in units of 10^{20} J) and conversion terms in units of 10^{14} J s^{-1}. These quantities have been evaluated between 1000 and 100 mb. The Southern Hemisphere quantities are restricted to the region north of 68°S.

	Northern Hemisphere			Southern Hemisphere	
	FGGE	NOSAT	STATIONS	FGGE	NOSAT
K_M	2.24	2.35	2.07	1.30	1.33
K_{TE}	2.04	2.08	1.91	1.21	1.22
K_{SE}	.60	.64	.55	.32	.32
$C(K_{TE},K_M)$	.53	.59	.56	1.18	1.24
$C(K_{SE},K_M)$	.56	.51	.21	.19	.21
P_M	13.4	14.1	14.5	5.07	5.67
P_{TE}	1.31	1.48	1.63	.52	.61
P_{SE}	1.17	1.25	1.93	.20	.28
$C(P_M,P_{TE})$	4.71	5.21	3.54	1.78	3.08
$C(P_M,P_{SE})$	2.52	2.68	2.75	.28	.13
$C(P_M,K_M)$	2.21	.96	2.95	-.53	-1.85

Attachment A

Accumulation of the Gridded Data

The following procedures are performed independently for each analysis (FGGE and NOSAT). The terms are accumulated sums (at a grid point) of the following:

u - 1	u^2 - 6	uv - 11	q - 20
v - 2	v^2 - 7	uz - 12	q^2 - 21
z - 3	z^2 - 8	uT - 13	uq - 22
T - 4	T^2 - 9	vz - 14	vq - 23
ω - 5	ω^2 - 10	vT - 15	ωq - 24
		ωu - 16	
		ωv - 17	
		ωz - 18	
		ωT - 19	

q terms are 0 above 300 mb

Term 25: ω - count term; 1 if present, 0 if absent.

Each data value represents a sum for N days, of a specific term at a specific level, latitude and longitude

$$\sum_{time=1}^{N} \text{VALUE(time, level, latitude, longitude)}$$

The units used are as follows:

u - m/s

v - m/s

q - gm/gm

T - °C (not °K)

z - m (departure from standard heights)

The standard heights for levels are as follows:

1000 mb	113 meters
850	1457
700	3011
500	5572
400	7181
300	9159
250	10363
200	11784
150	13608
100	16206
70	18486
50	20632

The 12 levels are as follows:

level 1 - 1000 mb
level 2 - 850 mb
etc.

The latitudes are as follows:

lat 1	90°S
lat 2	86°S
lat 3	82°S
lat 23	2°S
lat 24	2°N
lat 25	6°N
lat 45	86°N
lat 46	90°N

Four extra terms are:

sea level pressure	- term 26	at level 13 (sea level)
surface pressure	- term 27	at level 14 (surface)
surface temperature	- term 28	at level 14 (surface)
surface specific humidity	- term 29	at level 14 (surface)

Each logical record contains data for one term at one latitude at one level for 72 longitudes.

In the following:

ILEV = level number	NLEV = number of levels (=12)
ILAT = latitude number	NLAT = number of latitudes (=46)
ITERM = term number	NTERM = number of terms (=25)

A logical record has 73 words:

word 1 - header (INTEGER)

10000 * ILEV + 100 * ILAT + ITERM

words 2-73 (REAL*4)

data values at 72 longitudes

Records with sea level pressure, surface pressure and temperature, and surface specific humidity, precede the other terms. The other records are ordered sequentially by header word.

The data can be read by the following program:

```
      DIMENSION DATA(73), VALUE(72)
      INTEGER IHEADR
      EQUIVALENCE (IHEADR, DATA(1)), (VALUE(1), DATA(2))

      DO 200 K = 1,4                    } sea level pressure
      DO 100 ILAT = 1,NLAT              } surface pressure
100   READ DATA(I), I = 1,73            } surface temperature
200   CONTINUE                          } surface specific humidity
```

```
      DO 300 ILEV = 1,NLEV
      DO 300 ILAT = 1,NLAT
      DO 300 ITERM = 1,NTERM
300   READ DATA(I), I = 1,73          reads data values of 1st
                                      25 terms at 12 levels
```

One file of accumulated sums thus has

$$4 \times 46 + 12 \times 46 \times 25 = 13984 \text{ logical records}$$

The data are written in binary form with the following DCB specification:

```
RECFM = VBS, LRECL = 296, BLKSIZE = 29604
```

at 1600 BPI on a 9-track tape.

Attachment B

Gross Error Checks on STATION Input Data

1. Limits on height departure from standard height (see Attachment A)

Pressure (mb)	Max. height departure (m)
1000	400
850	600
750	1000
500	1000
400-50	2000

2. Limits on temperature values

Pressure (mb)	Min. T (°C)	Max. T (°C)
surface, 1000-300	- 82	50
250-50	-110	0

3. Limits on relative humidity values

Pressure (mb)	Min. RH	Max. RH
surface, 1000-300	0	100

4. Limits on wind values

a. Non-Russian stations

Pressure (mb)	Min. u (ms^{-1})	Max. u (ms^{-1})	Min. v (ms^{-1})	Max. v (ms^{-1})
surface, 1000-400	-100	100	-100	100
300-50	-100	125	-100	125

b. Russian Stations

All pressures $|u^2 + v^2| \leq 100$

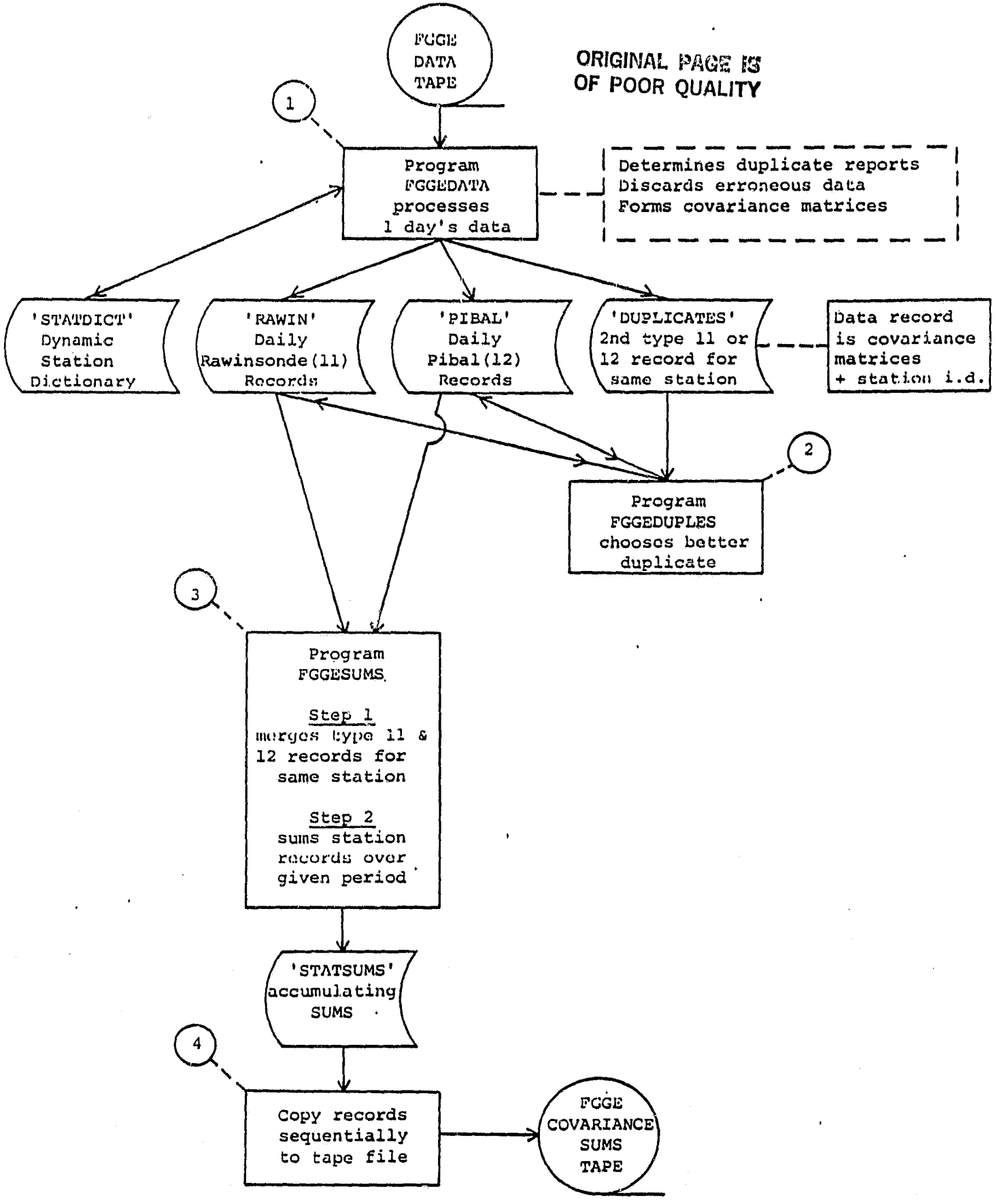

Figure 1. Flow Chart of Station Data Processing

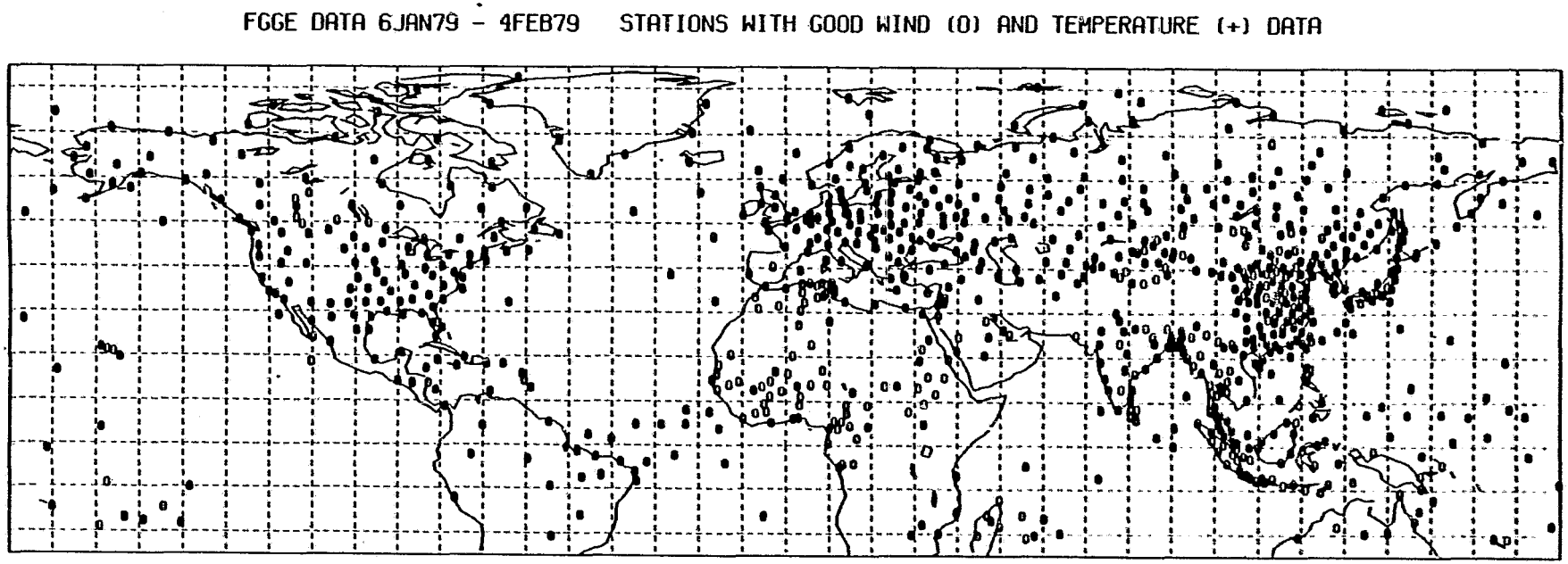

Figure 2a. Stations whose winds or temperatures at 850 mb pass cutoff criteria.

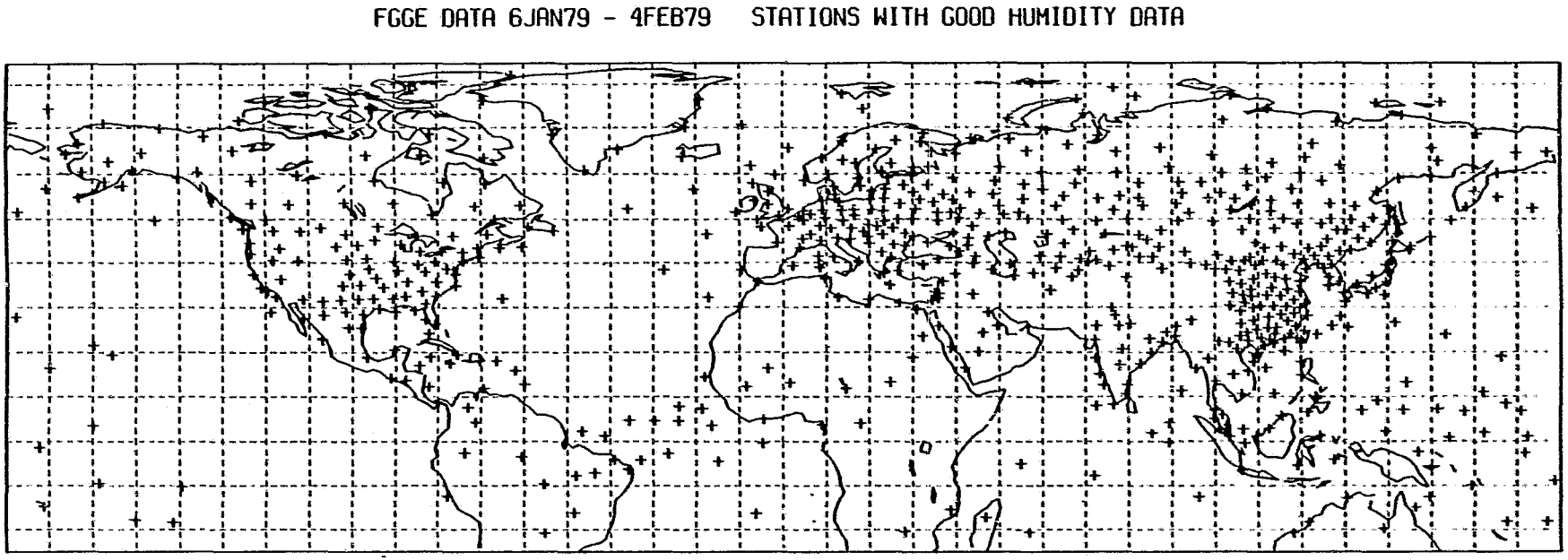

Figure 2b. Stations whose humidities at 850 mb pass cutoff criteria.

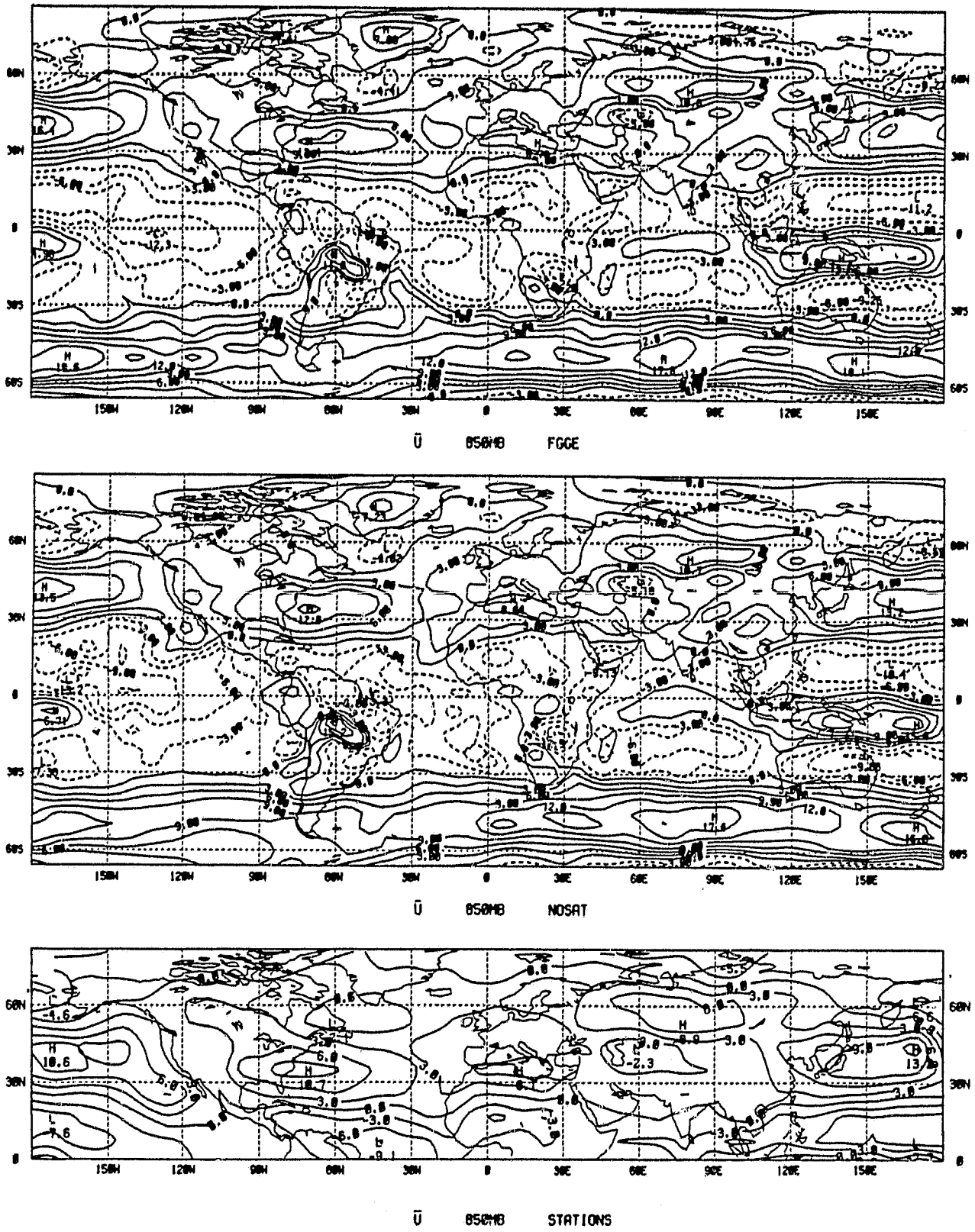

Figure 3. Zonal wind ($\bar{u}$) in m s^{-1} at 850 mb for the FGGE, NOSAT, and STATIONS analyses.

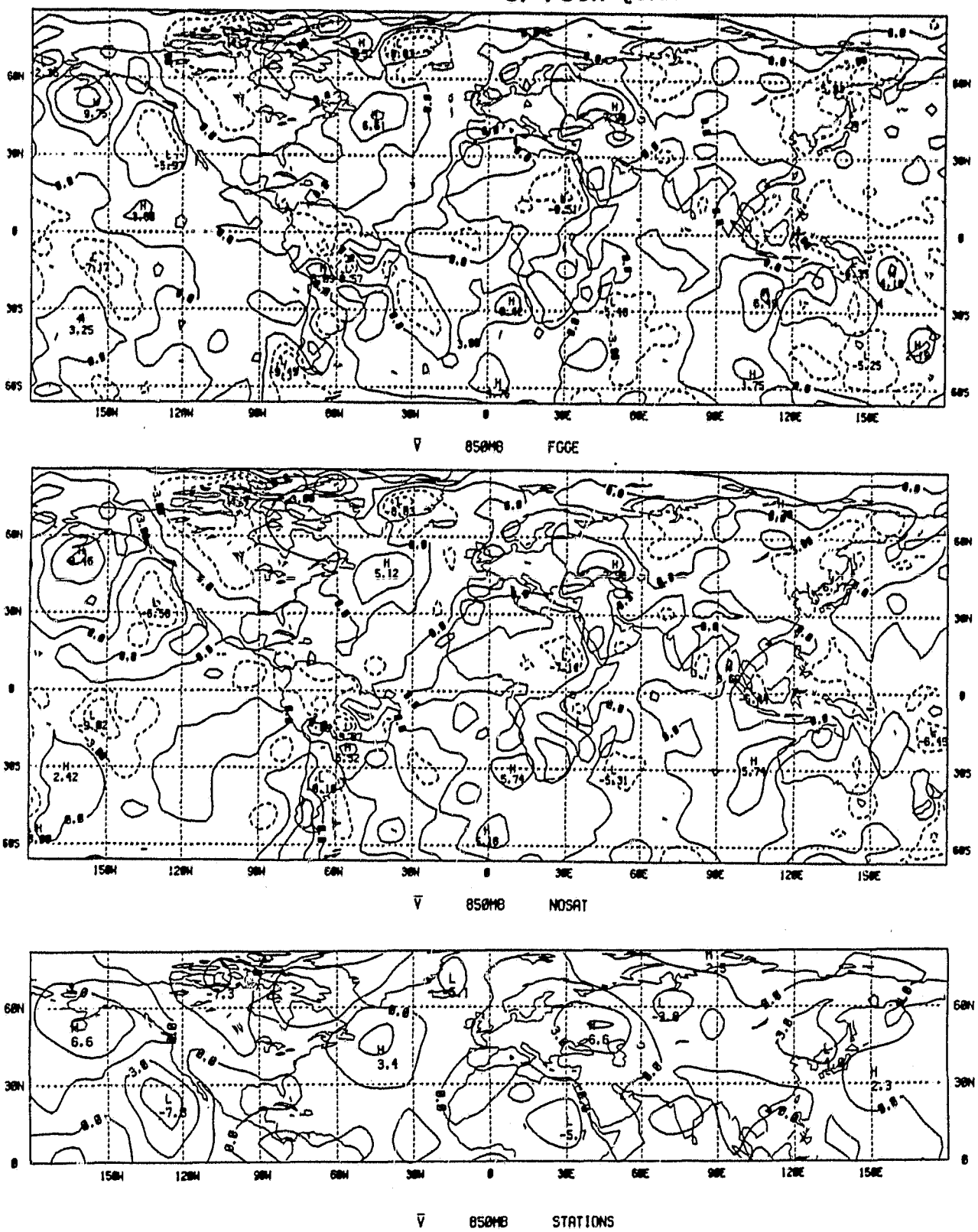

Figure 4. Meridional wind ($\bar{v}$) in ms^{-1} at 850 mb for the FGGE, NOSAT, and STATIONS analyses.

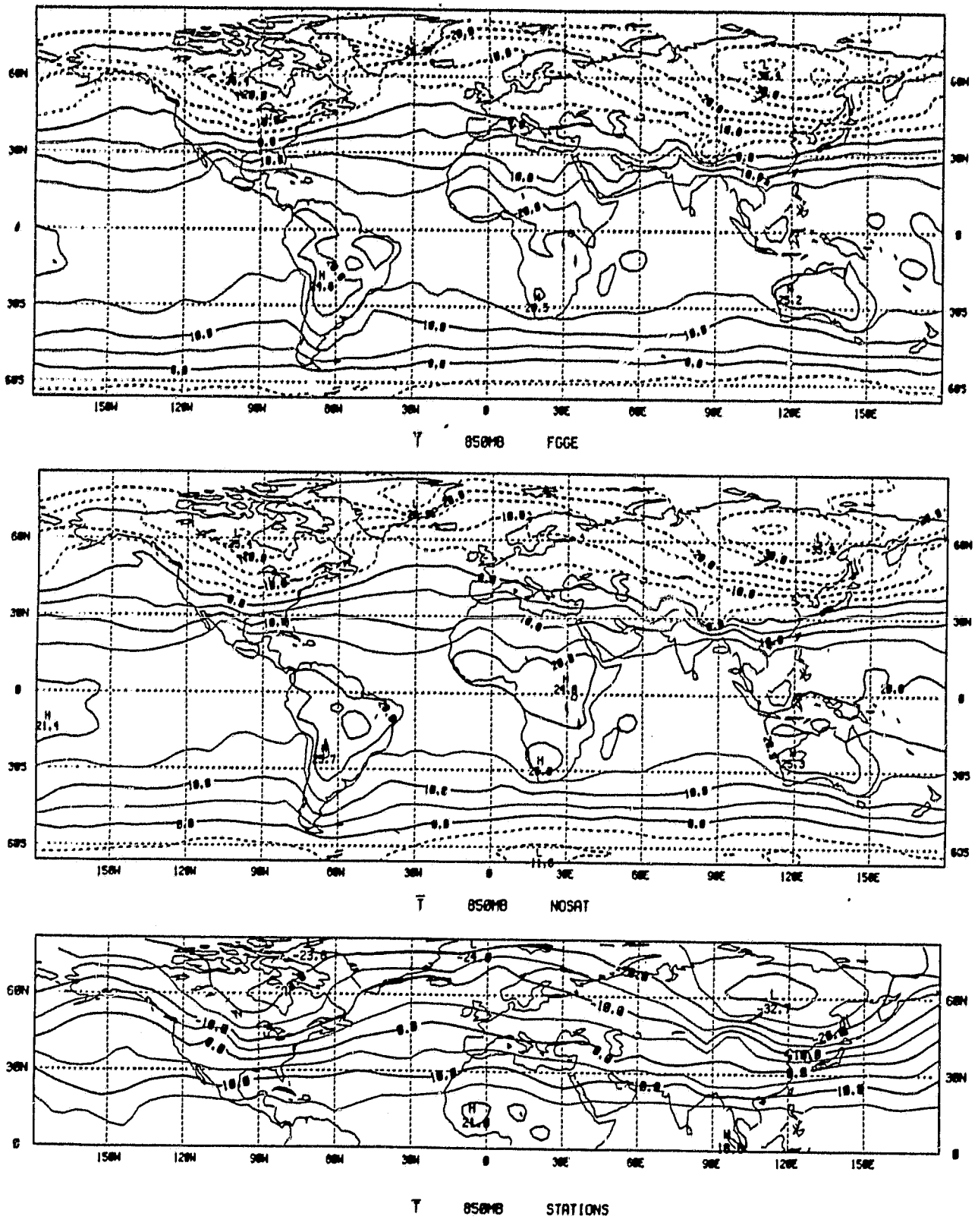

Figure 5. Temperature ($\bar{T}$) in °C at 850 mb for the FGGE, NOSAT, and STATIONS analyses.

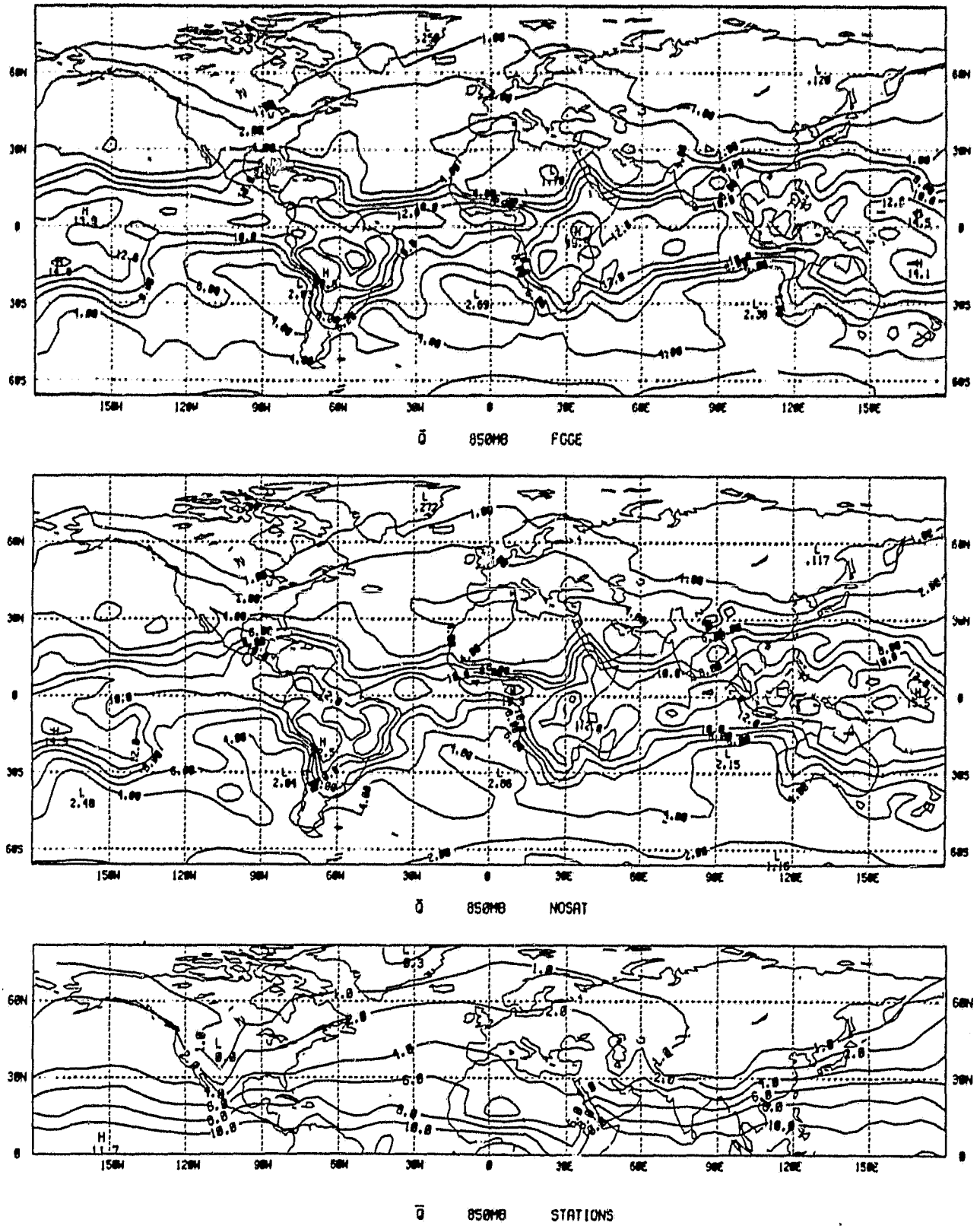

Figure 6. Specific humidity ($\bar{q}$) in gm kg^{-1} at 850 mb for the FGGE, NOSAT, and STATIONS analyses.

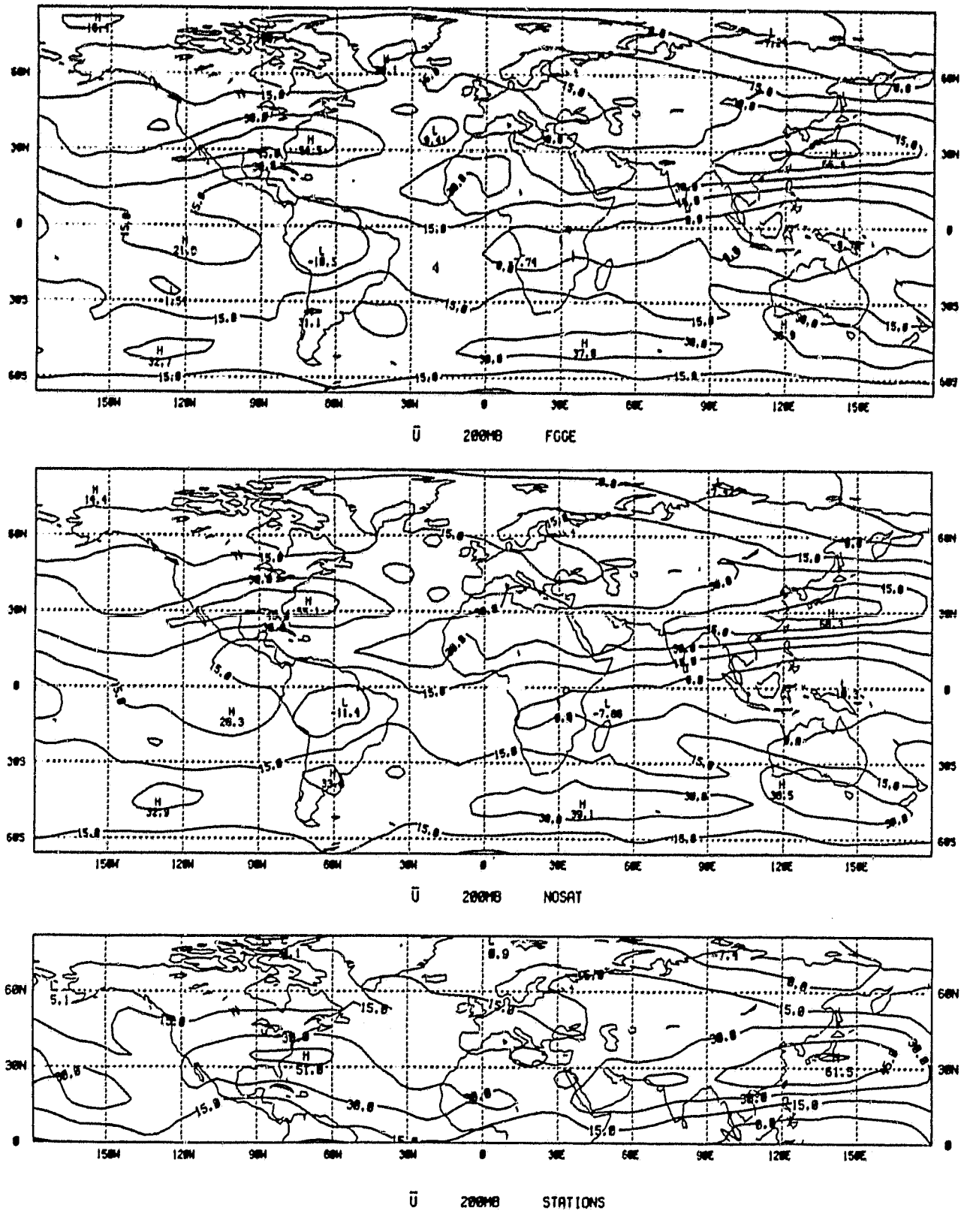

Figure 7. Zonal wind ($\bar{u}$) in ms^{-1} at 200 mb for the FGGE, NOSAT, and STATIONS analyses.

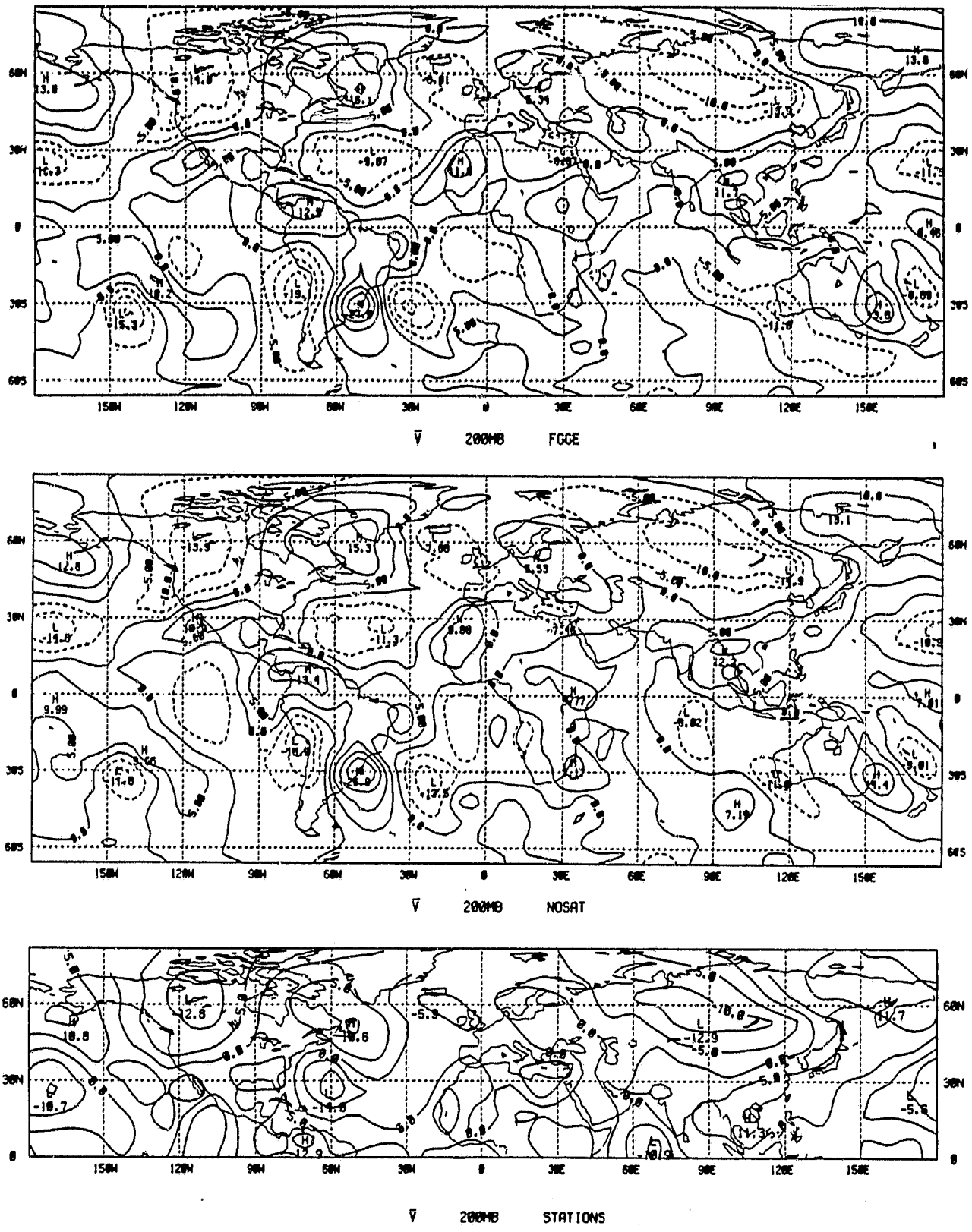

Figure 8. Meridional wind ($\bar{v}$) in ms^{-1} at 200 mb for the FGGE, NOSAT, and STATIONS analyses.

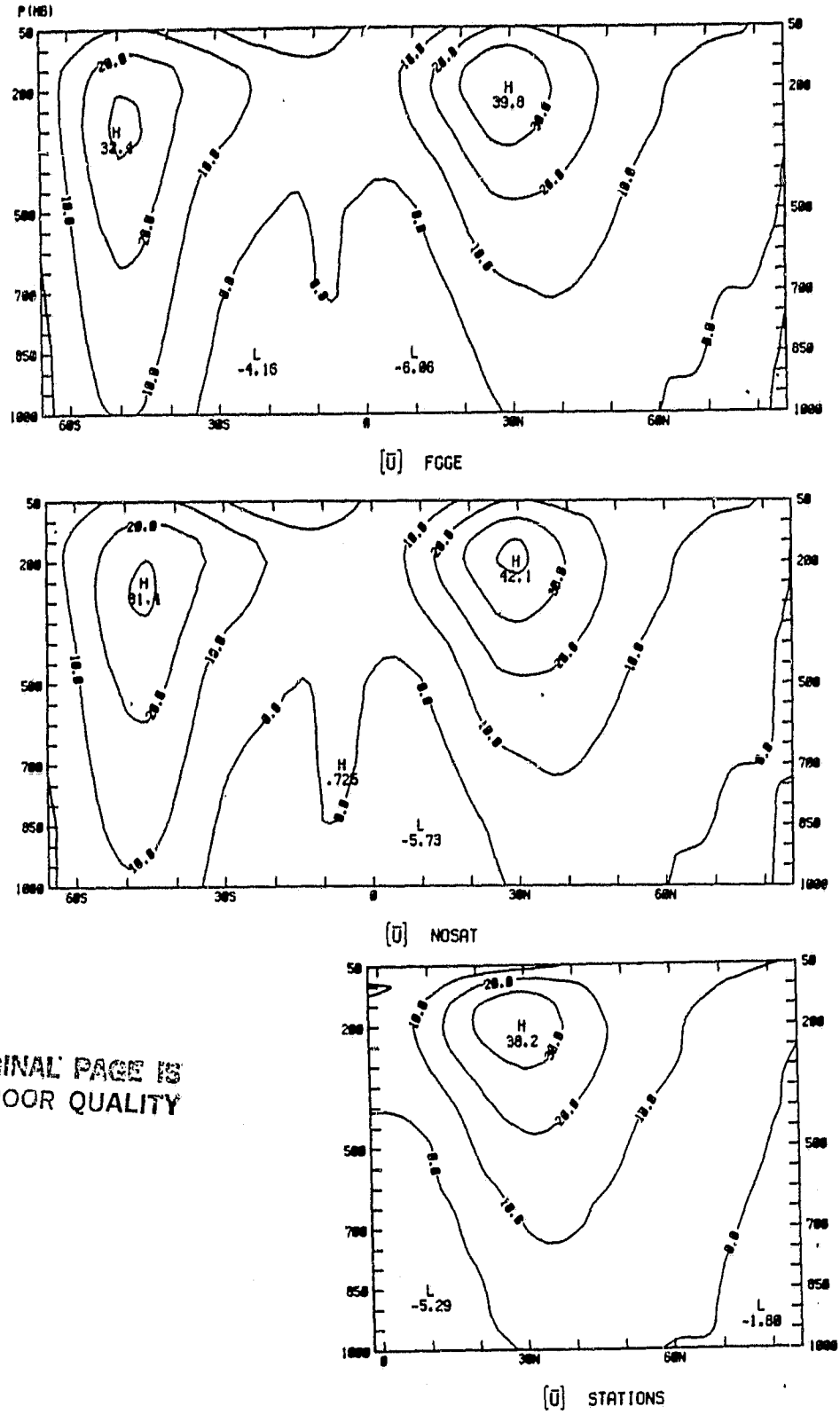

Figure 9. Zonally averaged zonal wind ($[\bar{u}]$) in ms^{-1} for the FGGE, NOSAT, and STATIONS analyses.

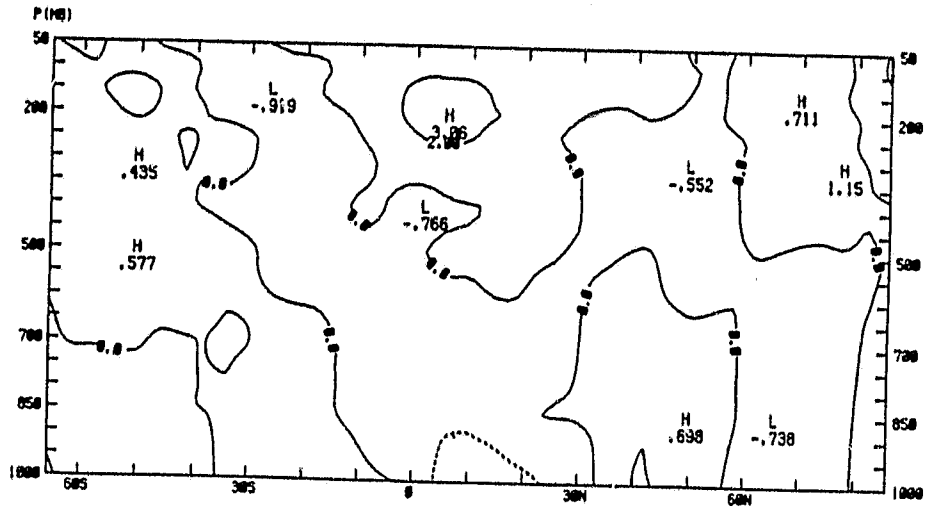

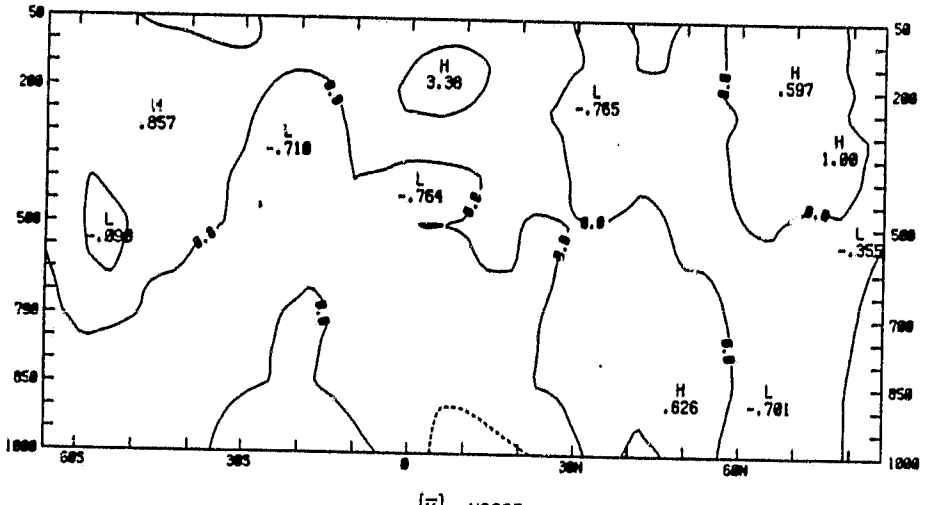

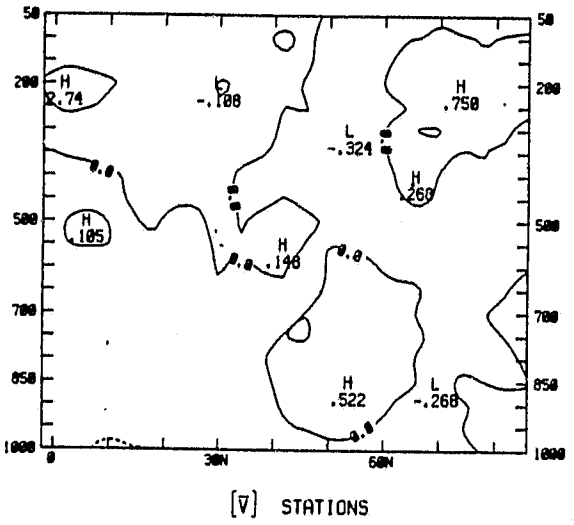

Figure 10. Zonally averaged meridional wind ($[\bar{v}]$) in ms^{-1} for the FGGE, NOSAT, and STATIONS analyses.

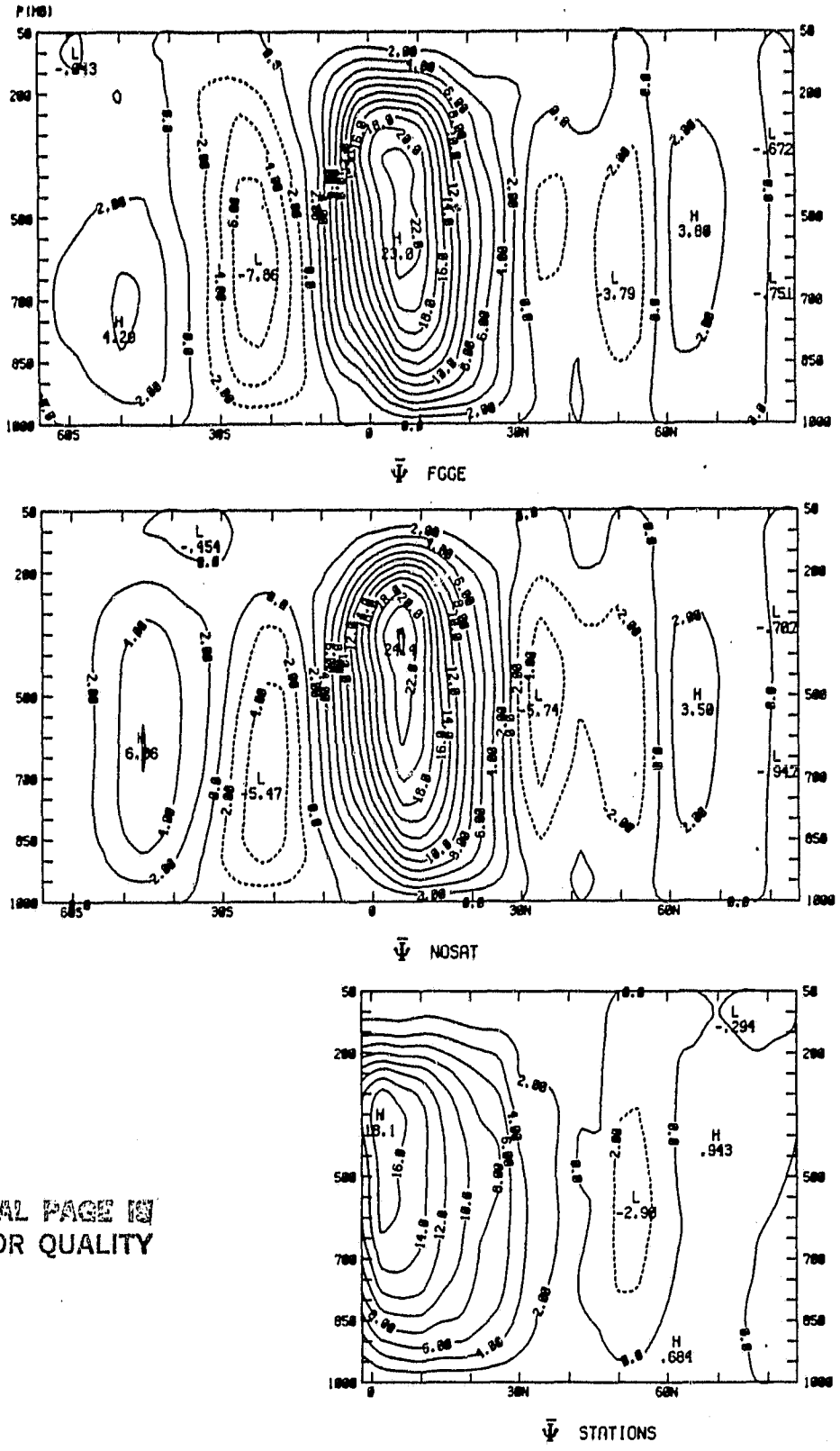

Figure 11. Mass streamfunction ($\bar{\Psi}$) in 10^{10} kg s^{-1} for the FGGE, NOSAT, and STATIONS analyses.

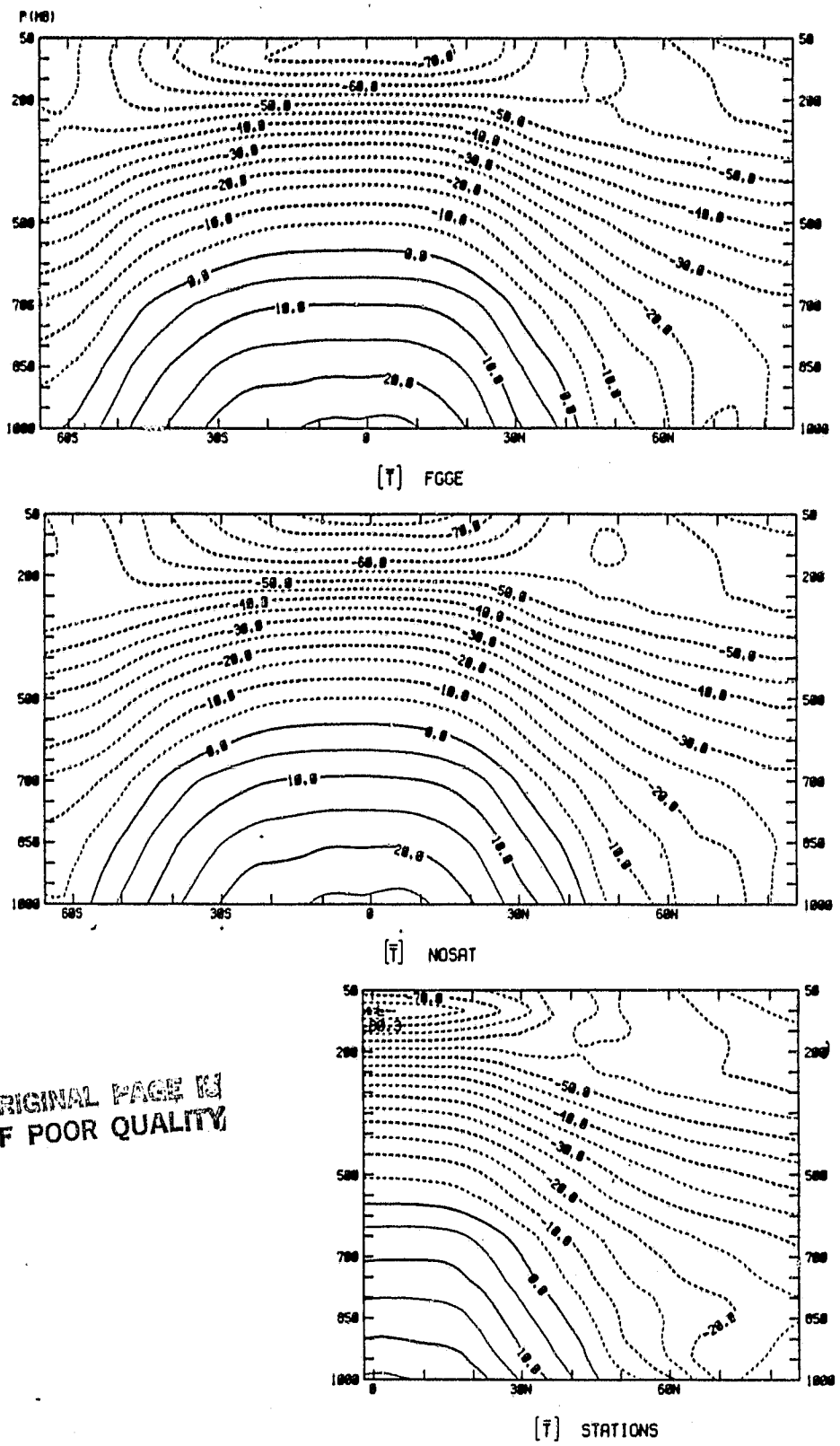

Figure 12. Zonally averaged temperature ($[\bar{T}]$) in °C for the FGGE, NOSAT, and STATIONS analyses.

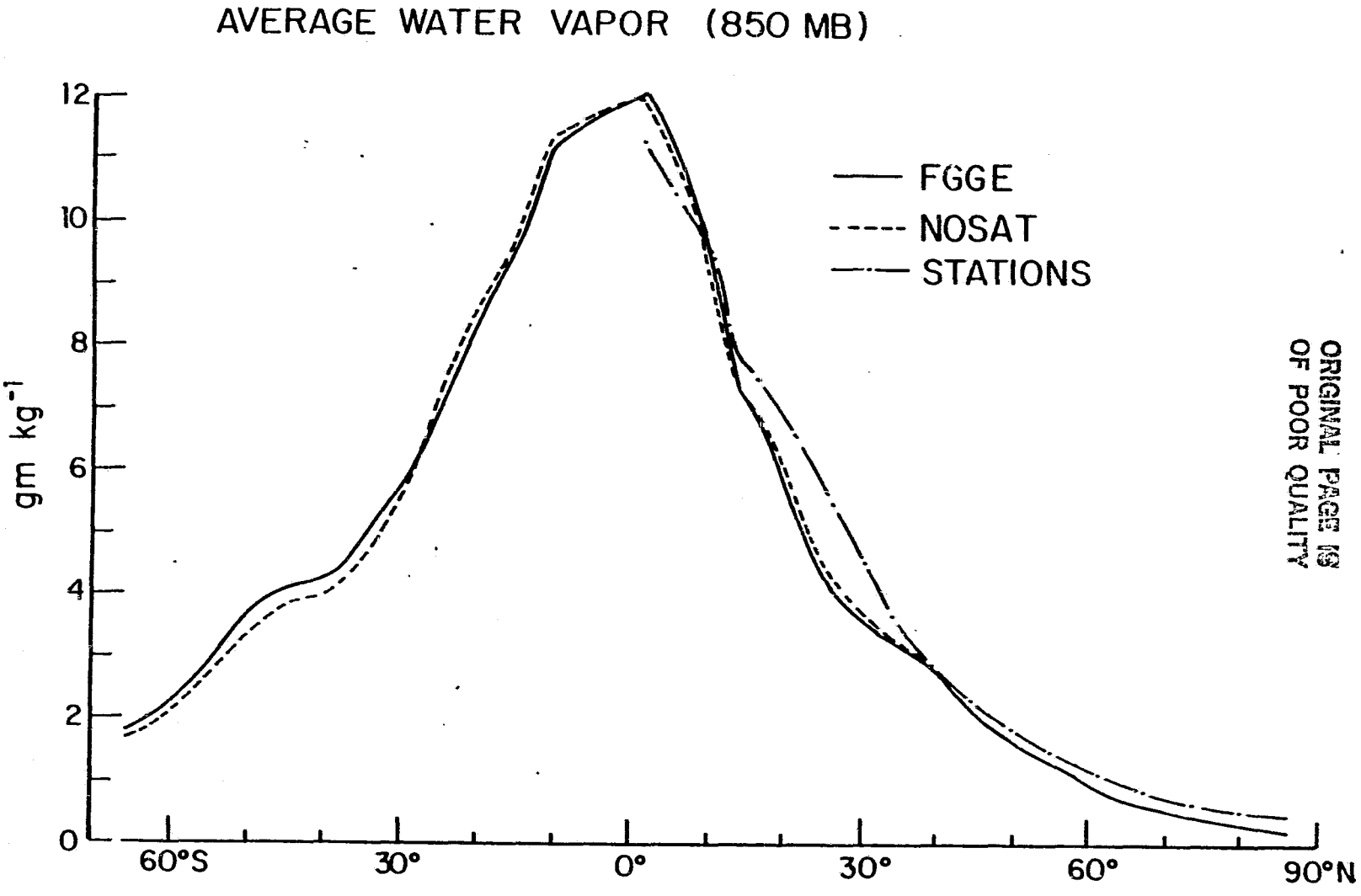

Figure 13. Zonally averaged water vapor ($[\bar{q}]$) in gm kg^{-1} at 850 mb for the FGGE, NOSAT, and STATIONS analyses.

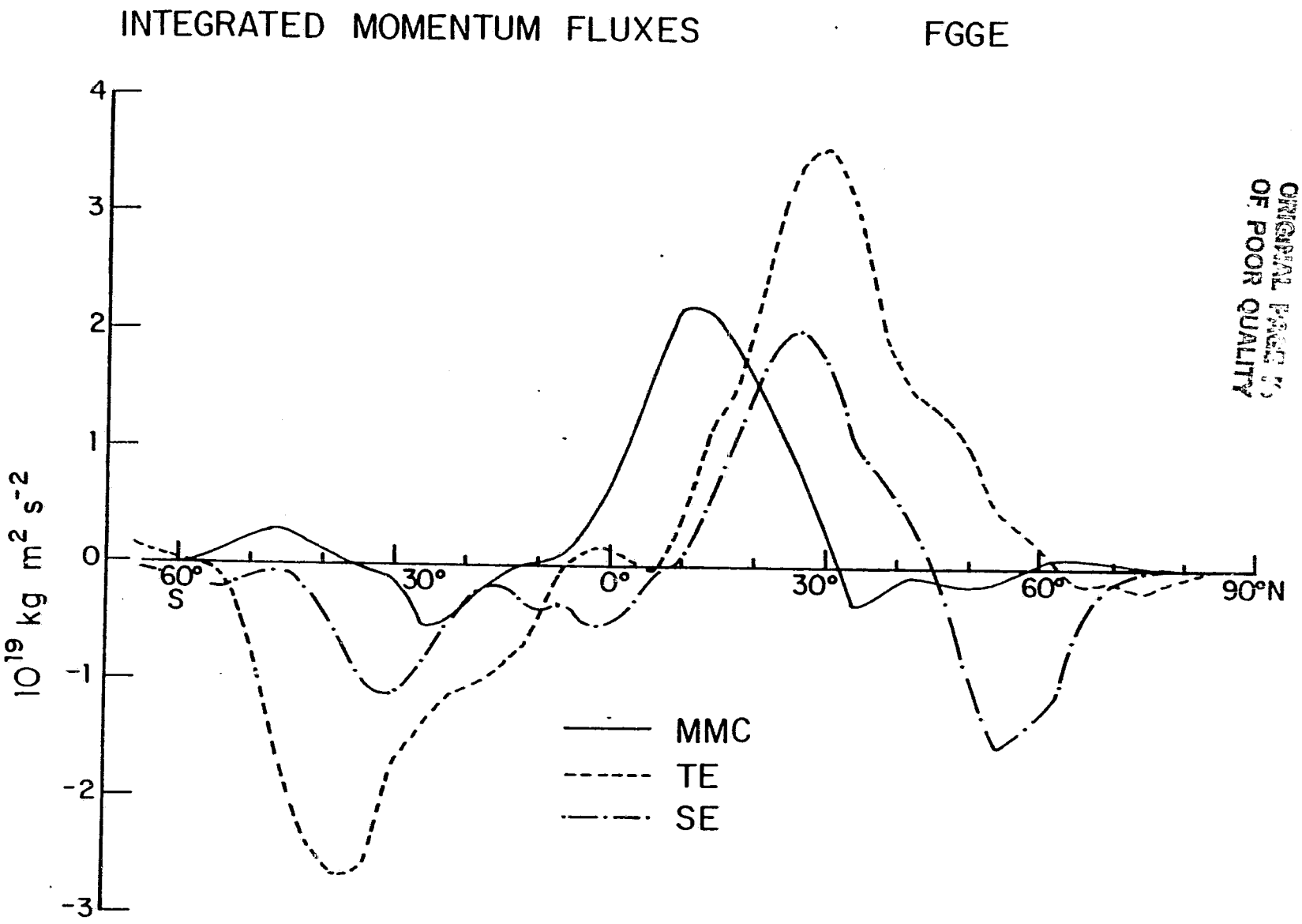

Figure 14a. Components of the vertically integrated northward momentum flux for the FGGE analysis.

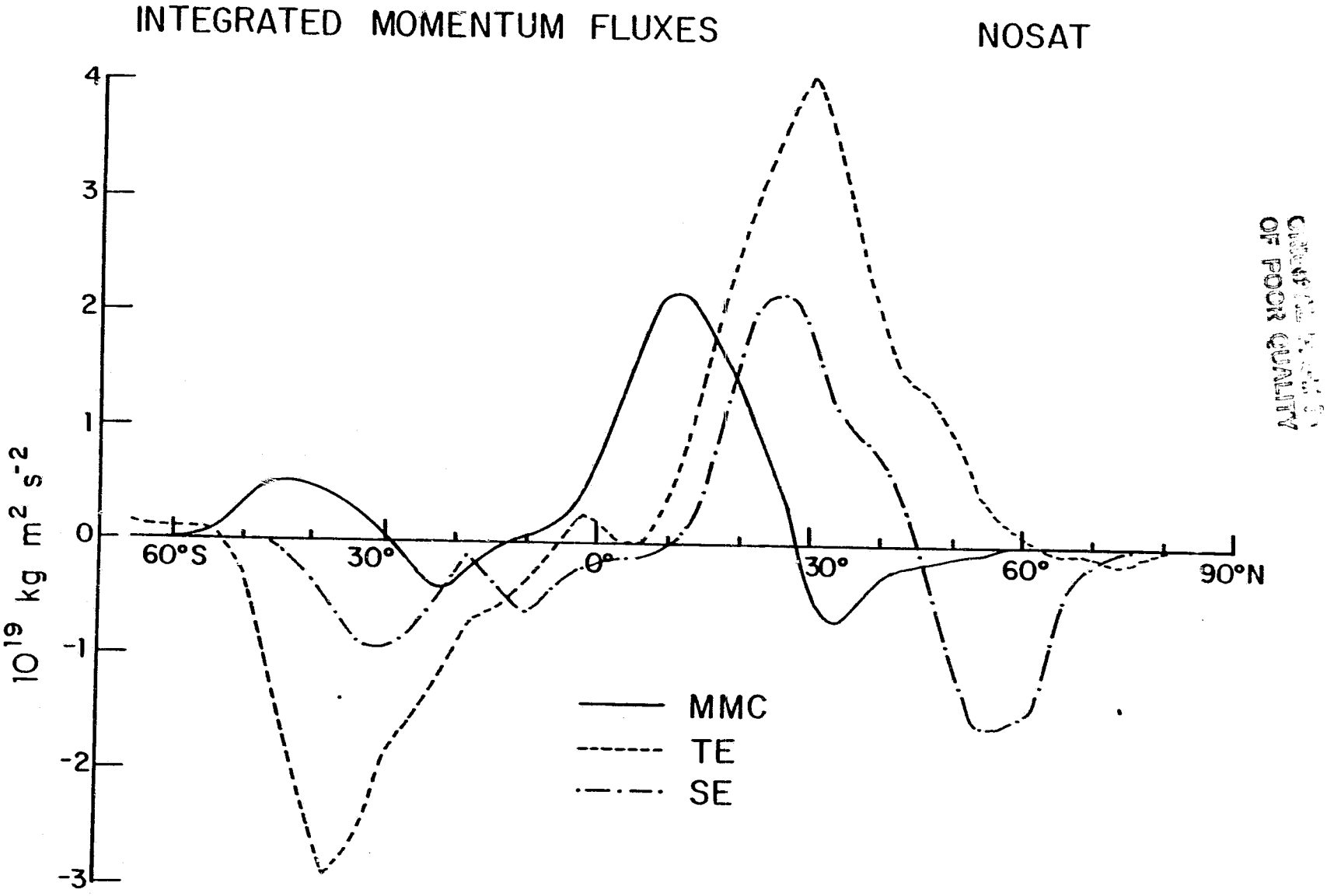

Figure 14b. Components of the vertically integrated northward momentum flux for the NOSAT analysis.

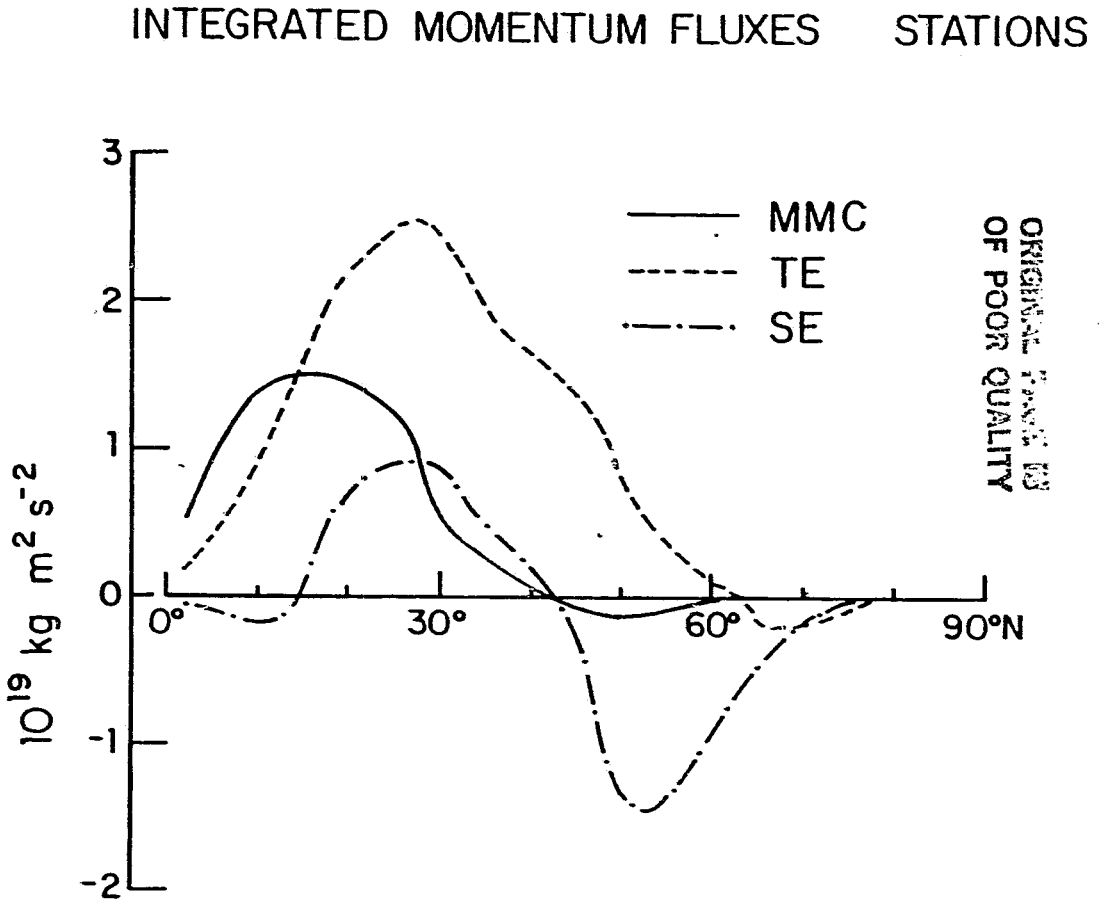

Figure 14c. Components of the vertically integrated northward momentum flux for the STATIONS analysis.

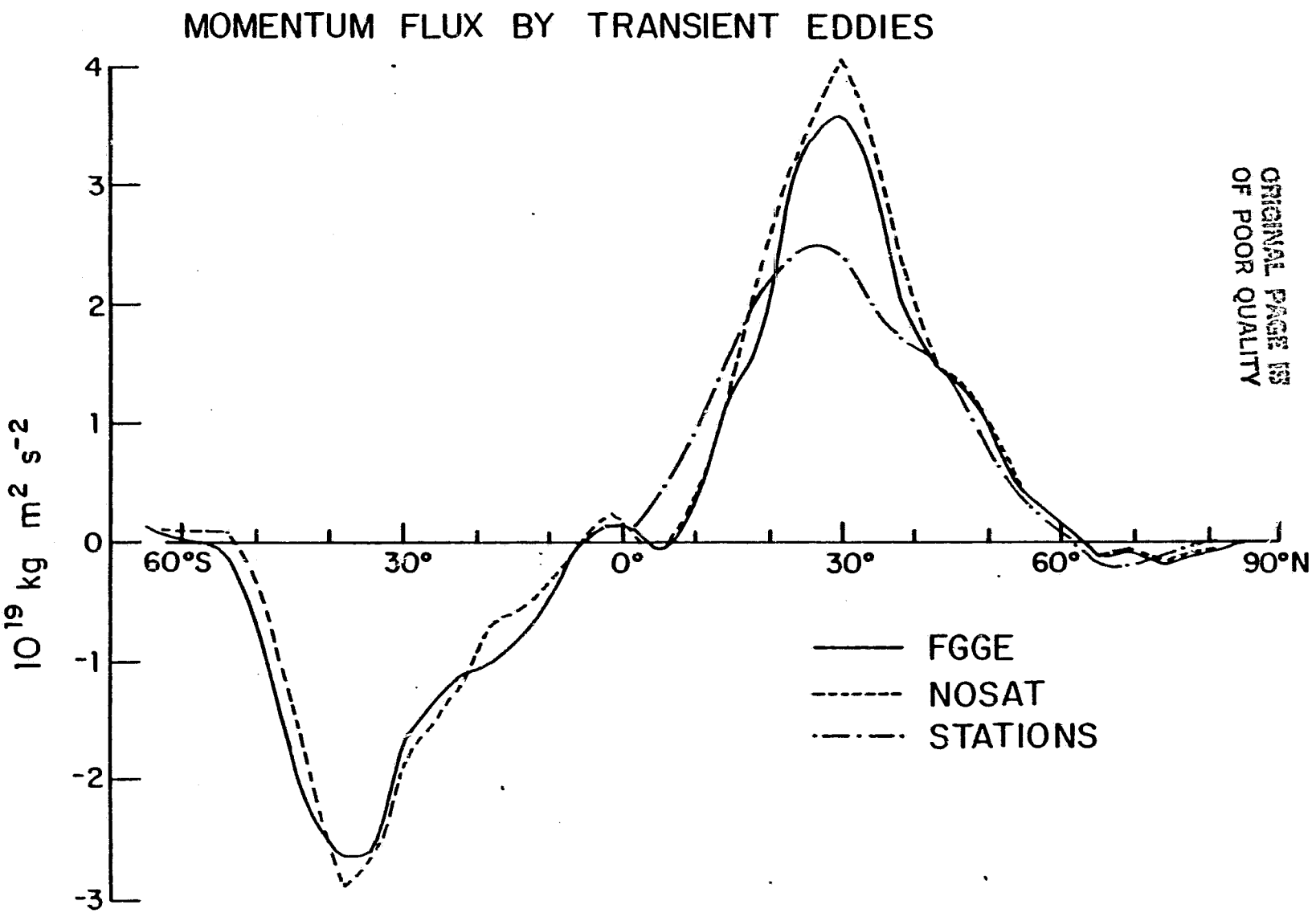

Figure 15. Vertically integrated northward momentum flux by the transient eddies for the FGGE, NOSAT, and STATIONS analyses.

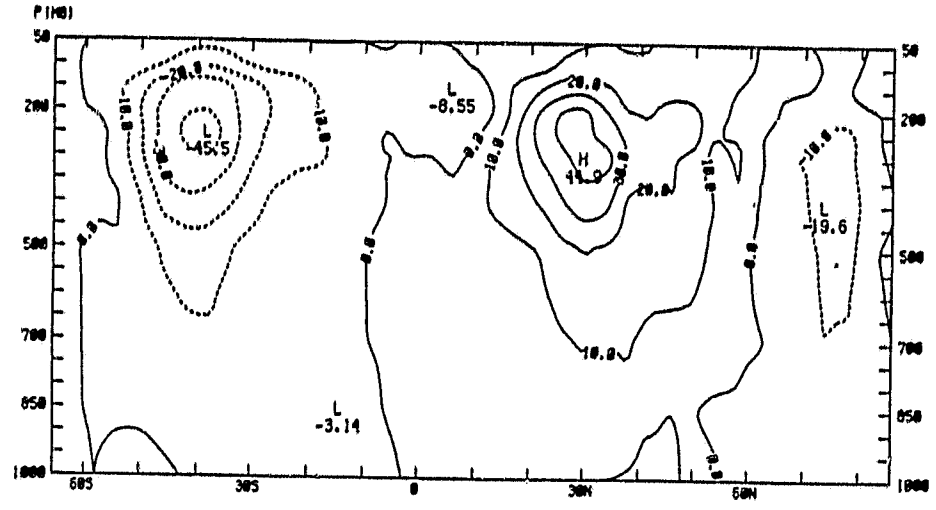

$[\overline{U'V'}]$ FGGE

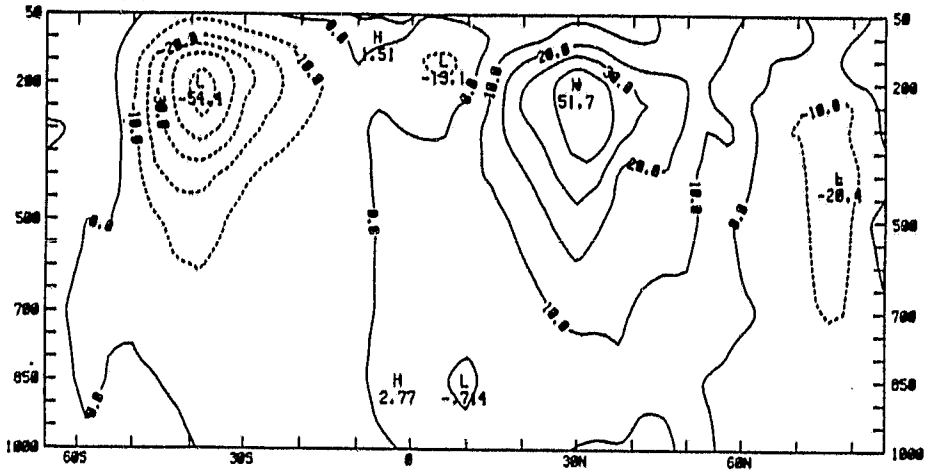

$[\overline{U'V'}]$ NOSAT

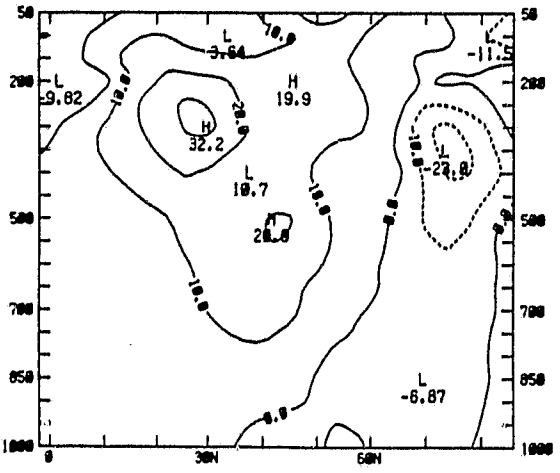

$[\overline{U'V'}]$ STATIONS

Figure 16. $[\overline{u'v'}]$ in $m^2 s^{-2}$ for the FGGE, NOSAT, and STATIONS analyses.

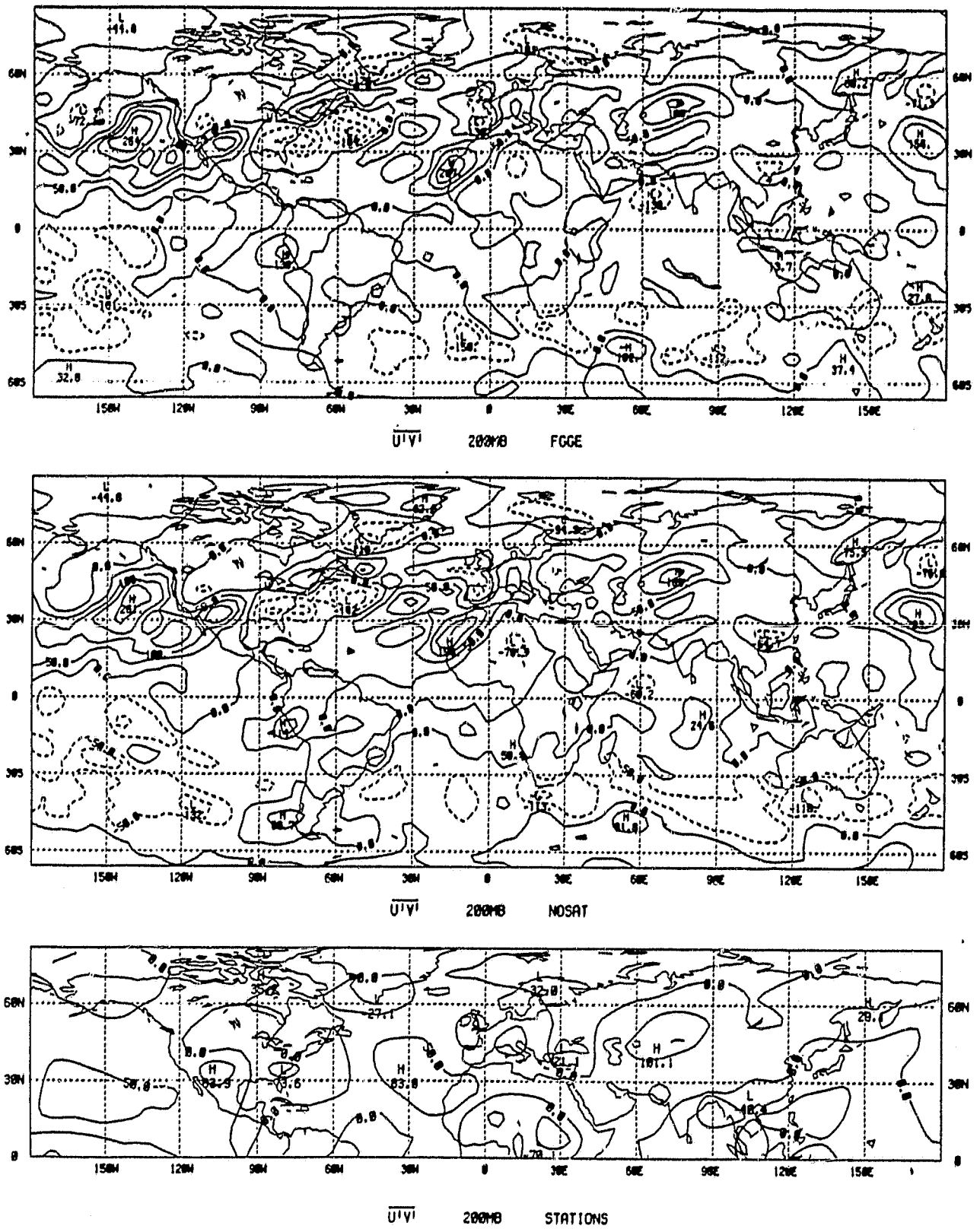

Figure 17. $\overline{u'v'}$ in $m^2 s^{-2}$ at 200 mb for the FGGE, NOSAT, and STATIONS analyses.

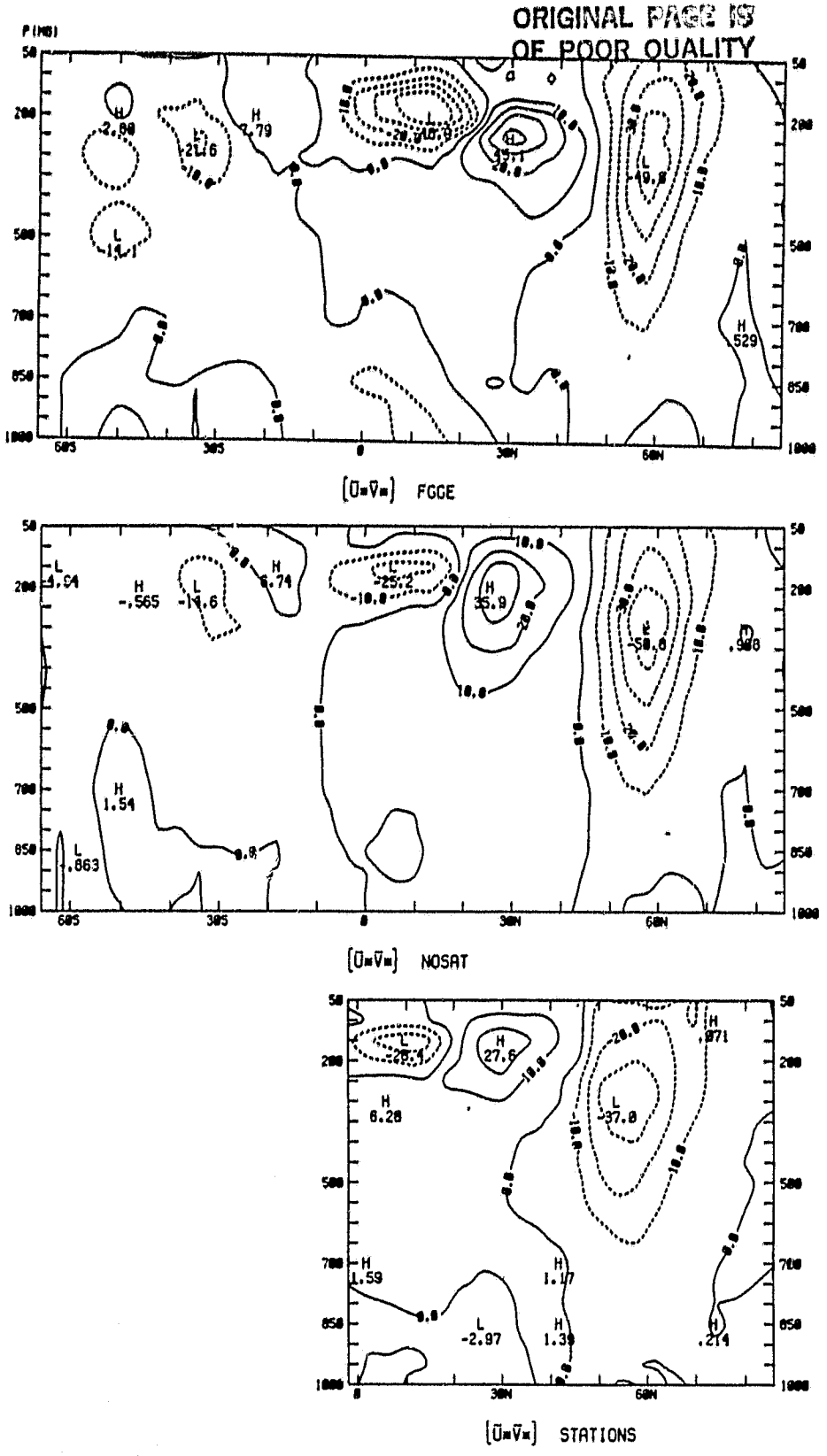

Figure 18. $[\bar{u}^*\bar{v}^*]$ in $m^2 s^{-2}$ for the FGGE, NOSAT, and STATIONS analyses.

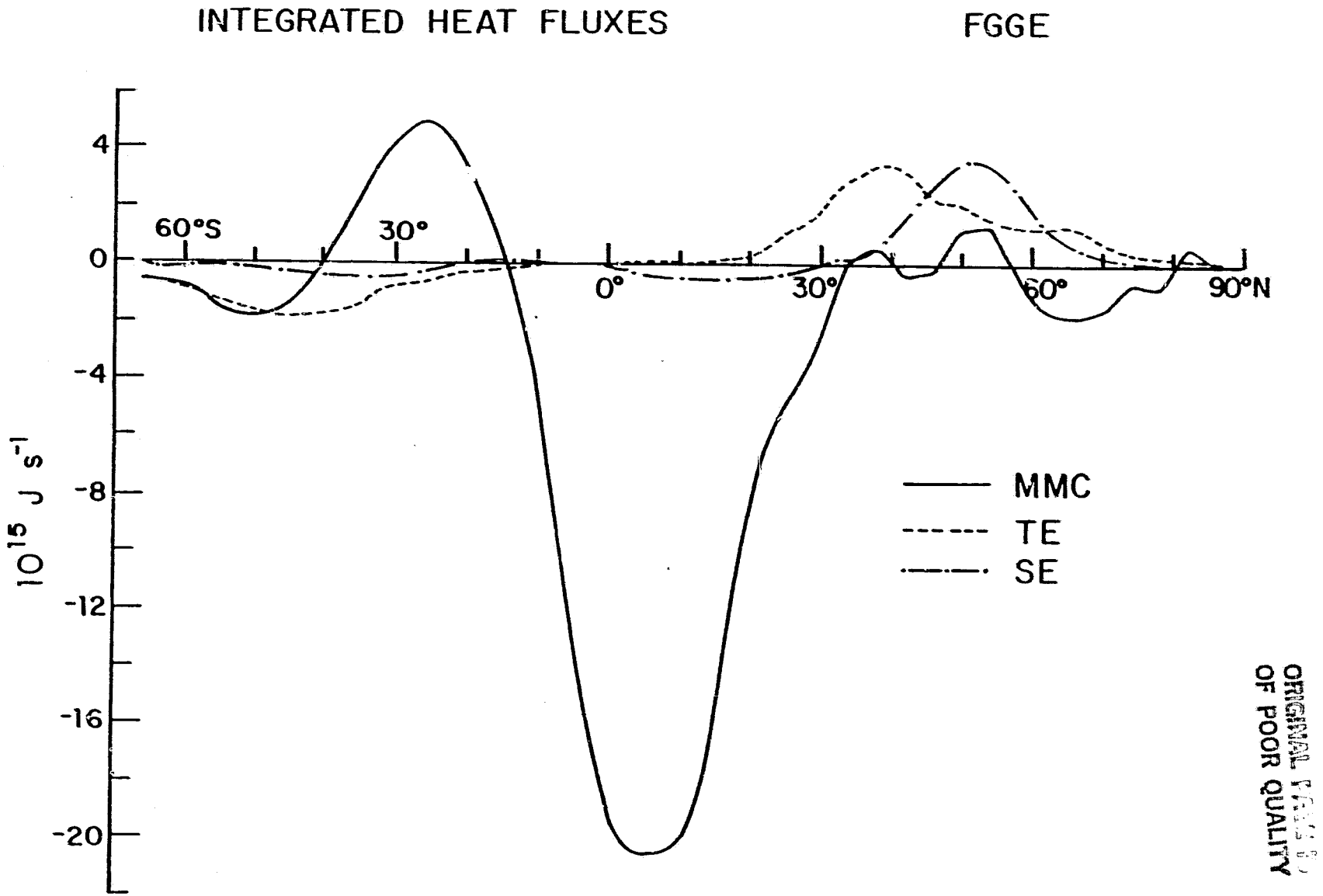

Figure 19a. Components of the vertically integrated northward heat flux for the FGGE analysis.

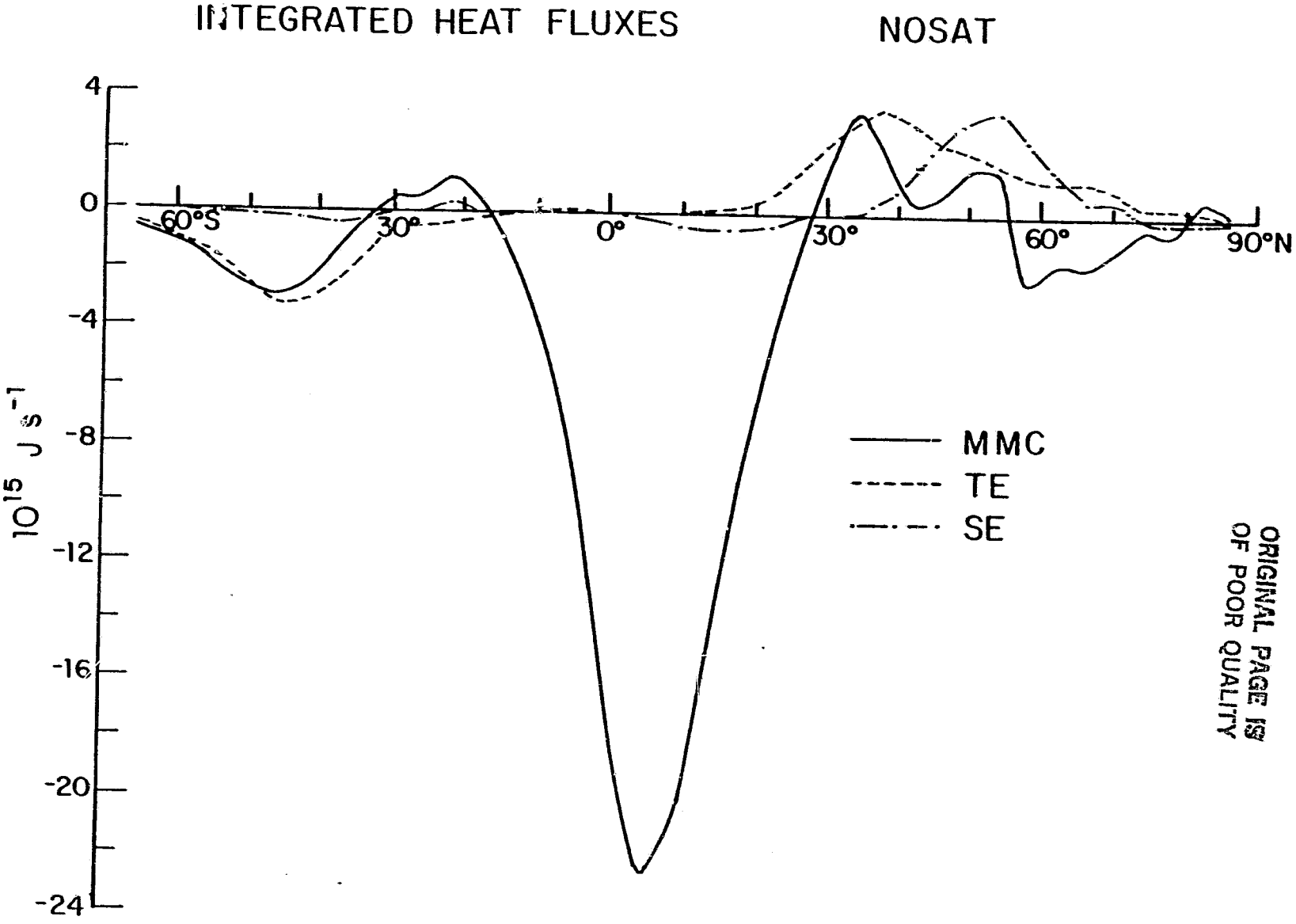

Figure 19b. Components of the vertically integrated northward heat flux for the NOSAT analysis.

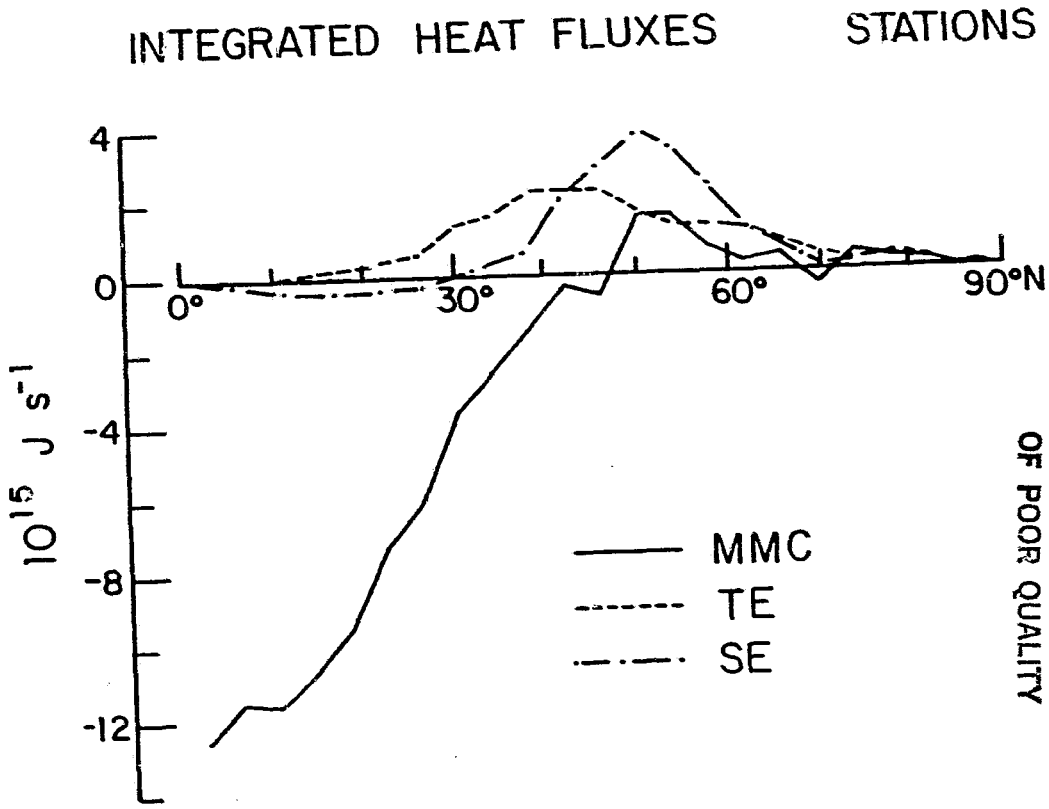

Figure 19c. Components of the vertically integrated northward heat flux for the STATIONS analysis.

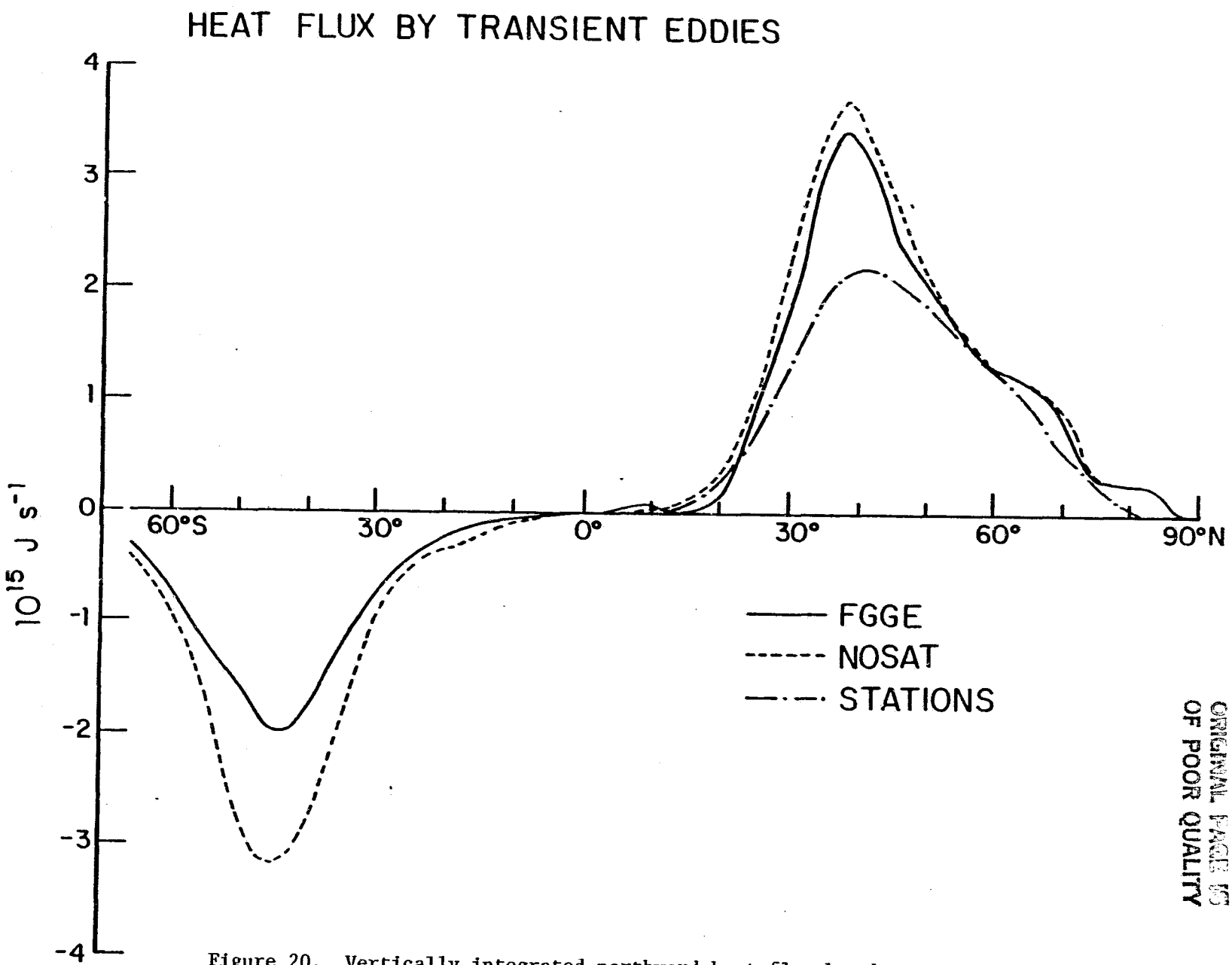

Figure 20. Vertically integrated northward heat flux by the transient eddies for the FGGE, NOSAT, and STATIONS analyses.

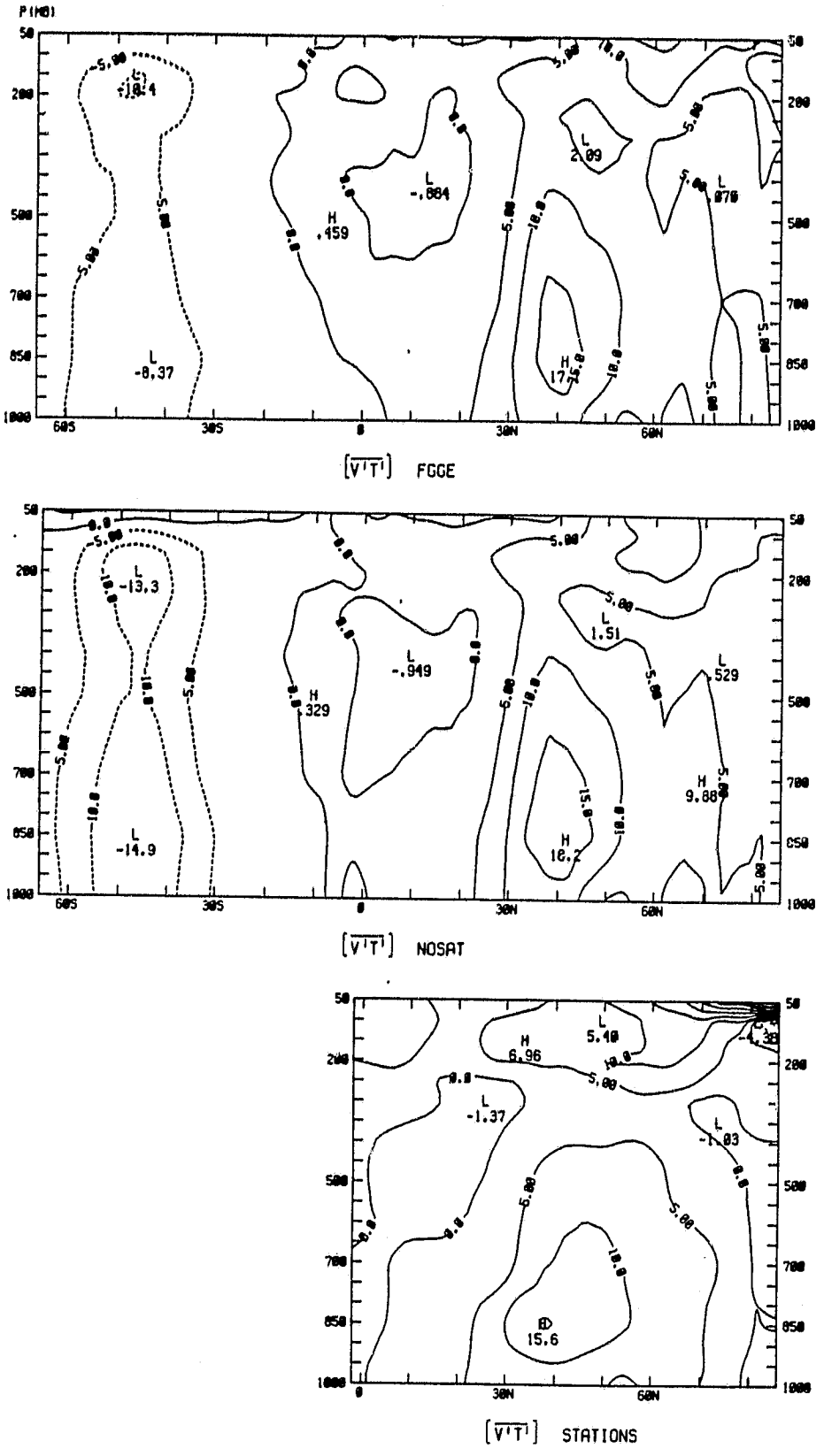

Figure 21. $[\overline{v'T'}]$ in $m^2 s^{-1}$ °C for the FGGE, NOSAT, and STATIONS analyses.

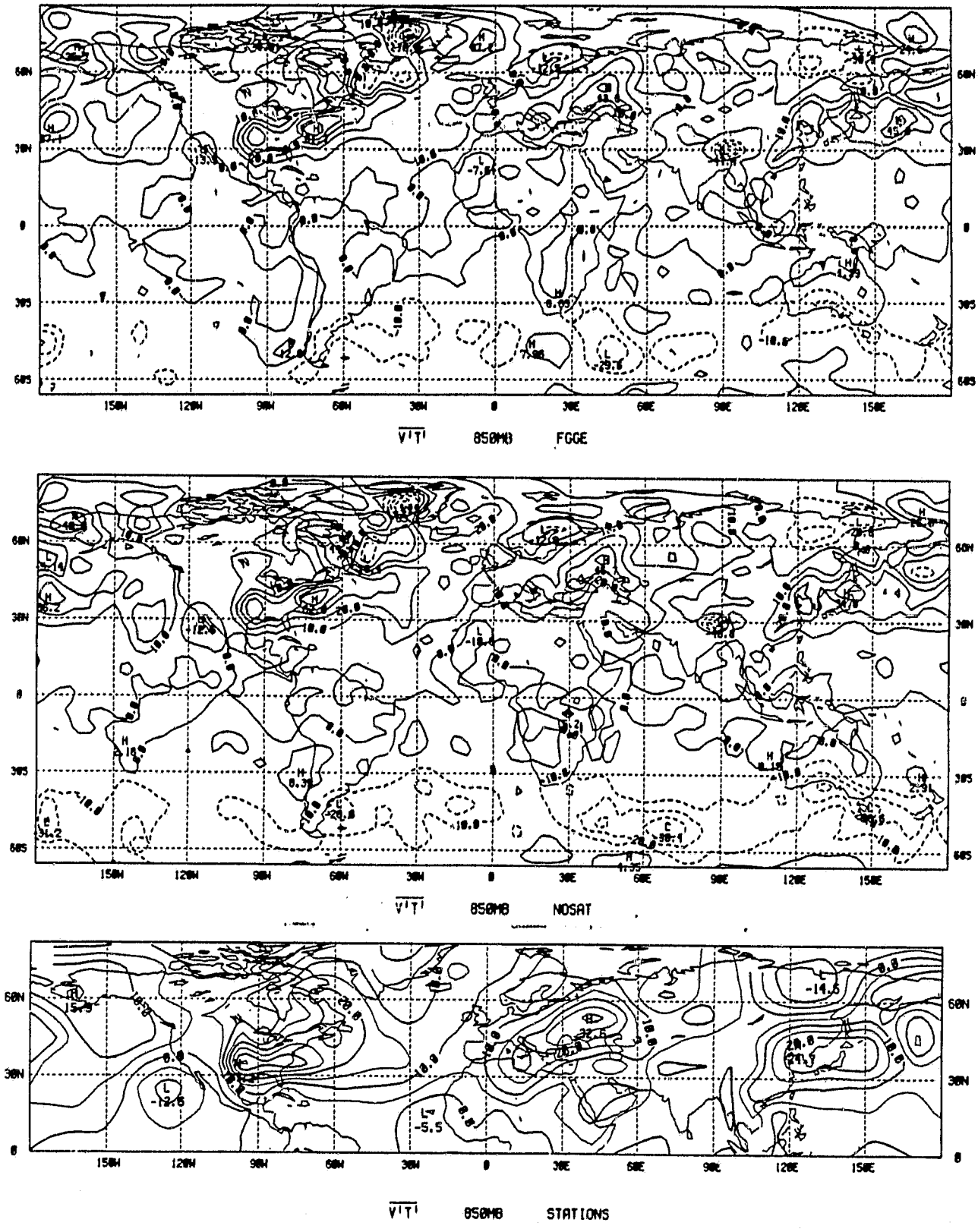

Figure 22. $\overline{v'T'}$ in $m^2 s^{-1}$ °C at 850 mb for the FGGE, NOSAT, and STATIONS analyses.

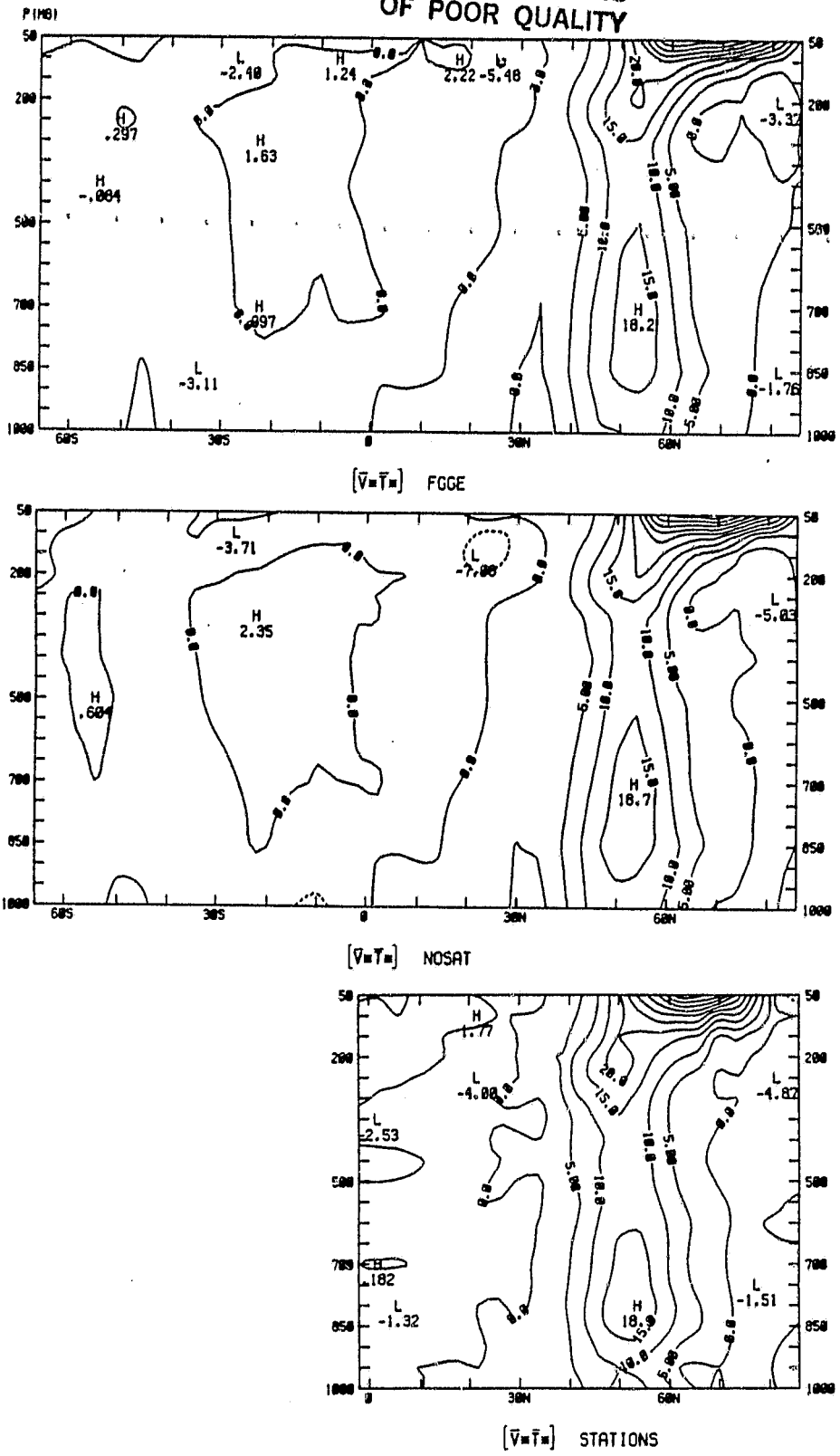

Figure 23. $[\bar{v}^*\bar{T}^*]$ in $m^2 s^{-1}$ °C for the FGGE, NOSAT, and STATIONS analyses.